Chapter 17
Power Architectures and Power Conditioning Unit for Very Small Satellites

Sergiu Oprea, Constantin Radoi, Adriana Florescu, Andrei-Stefan Savu and Adrian-Ioan Lita

Abstract Space agencies all over the world are interested today in very small satellites because of their advantages compared to heavier satellites. This chapter starts with the general characteristics, Earth orbits, eclipses and current missions of very small satellites. It continues with a brief summary of the component parts of the electrical power system: the array of solar cells, batteries for space applications, 3 power architectures and 19 maximum power point tracker's algorithms. Authors' attention is mainly focused on designing, simulation and practical demonstration of a prototype with a flexible hybrid proposed architecture of the power conditioning unit for very small satellites, whose component blocks are the battery charge unit (BCU) including the dc–dc converter, the digital controller, the BCU sensors circuitry and the BCU prototype) and the battery charge/discharge monitor unit (BCDMU) including the microcontroller, the BCDMU sensors circuitry, the battery switch, the battery heater and the telemetry system.

Keywords Very small satellites · Earth orbits and eclipses · Electrical power system · Flexible power architectures · Battery charger unit · Battery charge/discharge monitor unit

S. Oprea · C. Radoi · A. Florescu (✉) · A.-S. Savu · A.-I. Lita
University POLITEHNICA of Bucharest, Bucharest, Romania
e-mail: adriana.florescu@yahoo.com; adriana.florescu@upb.ro

S. Oprea
e-mail: oprea_serg@yahoo.com

C. Radoi
e-mail: conrad_1944@yahoo.com

A.-S. Savu
e-mail: savucfa@yahoo.com

A.-I. Lita
e-mail: adrian.lita@ieee.org

N. Bizon et al. (eds.), *Energy Harvesting and Energy Efficiency*,
Lecture Notes in Energy 37, DOI 10.1007/978-3-319-49875-1_17

Abbreviations and Acronyms

BCDMU	Battery Charge/Discharge Monitor Unit
BCU	Battery Charger Unit
BDR	Battery Discharge Regulator
BFV	Best Fixed Voltage
BOL	(Battery's) Beginning of Life
BU	Battery Unit
CCM	Continuous Current Mode
CMMR	Common Mode Rejection Ratio
COTS	Commercial-Off-The-Shelf
CU	Chargers Unit
DET	Direct Energy Transfer
DOD	Depth of Discharge
e.i.r.p.	equivalent isotropic radiated power
EOL	(Battery's) End of Life
ESA	European Space Agency
GEO	Geosynchronous Earth Orbit
GSTP	General Support Technology Programme
GUI	Graphical User Interface
HEO	Highly Elliptical Orbit
IC	Integrated Circuit
IOD	In-Orbit Demonstration
IU	Isolation Unit
LEO	Low Earth Orbit
LRCM	Linear Reoriented Coordinates Method
MEO	Mid Earth Orbit
MPPT	Maximum Power Point Tracker
NGSO	Non-Geostationary Orbit
NTC	Negative Temperature Coefficient
OCC	One-Cycle Control MPPT
P&O	Perturb and Observe
PEC	Packet Error Check
PI	Proportional-Integral
POL/D	Point-Of-Load/Distribution
PV	Photovoltaic
PWM	Pulse Width Modulation
RCC	Ripple Correlation Control
S3R	Sequential Switching Shunt Regulator
SEPIC	Single-Ended Primary Inductor Converter
STAR	Space Technology and Advanced Research
TT&C	Telemetry, Tracking and Telecommand

17.1 Introduction in Very Small Satellites

The spaceflight literature defines today the artificial satellite (usually, simply called satellite) as an object placed on purpose into a space orbit to fulfill a specific mission [1]. Small satellites, also known as miniaturized satellites, are defined as low mass satellites (up to 500 kg) and small size [2]. The definition of very small satellites varies today, sometimes gathering together micro-, nano-, pico- and femto-satellites [3], sometimes defining only nanosatellites and picosatellites (such as CubeSats) [4], sometimes including all small satellites having under a kilogram mass [5] etc.

Many reasons justified small and very small satellites to appear and develop:

- big amount of energy saving
- to lower the cost of the existing heavier satellites, that impose massive rockets to make possible the launch operation in space and possibility of multiple launch;
- to allow with few finance in formation flight of a small satellites cluster;
- to allow low cost design;
- to make easier the mass production;
- to facilitate not solvable missions by larger satellites, such as:
  - formations missions dedicated to low data rate communications;
  - data collection missions from multiple points that need formation flights;
  - in-space inspection and service for larger satellites placed in orbit;
  - research and design missions for universities.

Today the very small satellites become a usual presence in space. A significant increase of the number of space experiments is also observed. As a direct consequence of these, are the increased demands and technical challenges for the power system. The miniaturized satellites standards like the “nanosat” or “picosat” push the limits even harder: the engineers face the problem of designing in a restricted space, with a limited amount of the available energy and financial resources while satisfying in the same time the criteria of maximum capabilities and performances.

17.1.1 Characteristics of Small Satellites

The block diagram in Fig. 17.1 points out the mandatory systems present in any satellite in order to accomplish the proposed mission (marked with solid lines) and its essential supporting systems (marked with intermittent lines).

In terms of spacecrafts, these systems are usually known and clustered as: the payload and the bus. The payload refers to the main communications equipment/science instruments for the commercial/research satellites. The bus gathers all the other essential systems that assist the payload such as: the electrical power system, the communications and data coordinating systems, all on-board telemetry sensors, the main satellite’s computer etc.

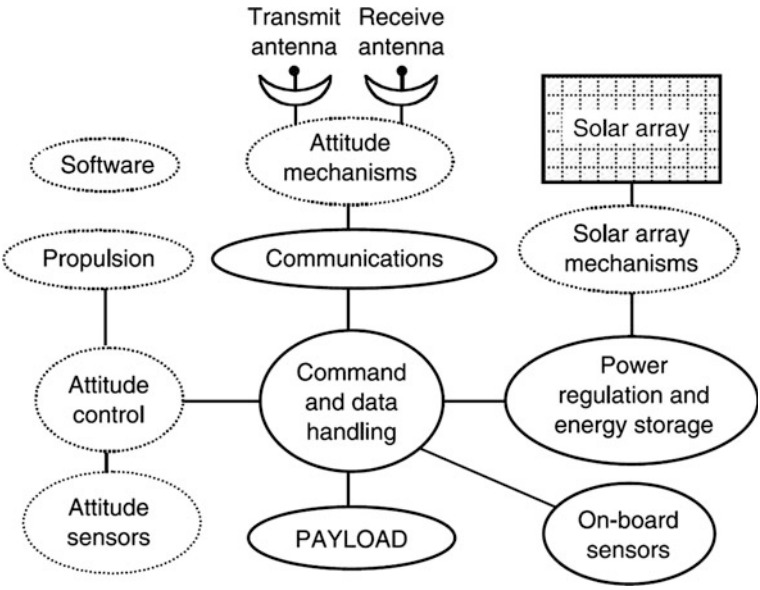

Fig. 17.1 Satellite systems

The electrical power system contains: the solar array as satellite's primary electric source of energy, the batteries to store and regulate this energy and all their associated power electronics to convert, control and distribute the electric energy to the payload [6]. A part of the electrical power system for very small satellites, namely the power conditioning unit, represents the subject of this chapter. Usually, the most popular theoretical approach to sort small satellites is by their mass, as shown in Table 17.1, where the presented values are just for reference and were taken according to the year 2014. In space field, a satellite may have different characteristics and still be in one of the presented categories.

Aside from size and/or mass and the other typical classification criteria presented in Table 17.1, there are also some rather important factors such as orbital uncertainty, low satellite equivalent isotropic radiated power (e.i.r.p.) and speed of development [7].

17.1.2 The Earth Orbits

The Earth is almost a sphere with the mean radius of 6371.0 km, equatorial radius of 6378.1 km and the polar radius of 6356.8 km, that has a reduced flattening (as a measure of compression from sphere to spheroid) only of 0.0033528. Starting from the surface and up to 160 km in the air, Earth's atmosphere is present and then it gradually vanishes into the vast space [6].

Table 17.1 Typical classification criteria of small satellites

Satellite's category	Mass (kg)	Maximum bus power (W)	Typical costs (USD)	Maximum dimensions (m)	Development time (years)	Orbit types	Mission endurance (years)
Minisatellite	100–500	1000	30–200 M	3–10	3–10	GEO MEO LEO HEO	5–10
Microsatellite	10–100	150	10–150 M	1–5	2–5	LEO (HEO)	2–6
Nanosatellite	1–10	20	100 k–10 M	0.1–1	1–3		1–3
Picosatellite	0.1–1	5	50 k–2 M	0.05–0.1			
Femtosatellite	< 0.1	1	<50 k	0.01–0.1	1		<1

Table 17.2 The Earth orbits and their major characteristics

Orbit	Apogee[a] (km)	Perigee[b] (km)	Eccentricity[c]	Inclination[d] (°)	Perioad[e]
GEO	35,786	35,786	0	0	1 sidereal day
GSO	35,786	35,786	0	0–90°	1 sidereal day
LEO	Variable	Variable	0–High	0–90°	>90 min
HEO	39,400	1000	High	62.9°	1/2 sidereal day

[a] Closest distance from the Earth surface
[b] Farthest distance from the Earth surface
[c] Ratio of difference to sum of apogee and perigee radii
[d] Angle between orbit plane and equatorial plane
[e] One sidereal day is 23 h, 56 min, 4.09 s

The Earth orbits of the artificial satellites are mentioned in Table 17.2 with their major characteristics. The standard abbreviations of these orbits are:

- GEO Stationary (abbreviated GEO): the Earth Orbit with an orbital period the same as the Earth's rotation period, placed above the Earth's equator
- GEO Synchronous (abbreviated GSO): the Earth orbit which enables to be synchronized with the rotation of the Earth
- MEO: mid Earth orbit, circular at 2000–20,000-km altitude
- LEO: low Earth orbit, generally circular at 200–2000-km altitude
- HEO: highly elliptical orbit, such as Molniya.

Van Allen radiation belts, depicted in Fig. 17.2, represent layers of energetic charged particles coming from the solar wind and cosmic rays, which are held in place by Earth's magnetic field [8]. The inner belt is formed by o combination of many protons and less electrons and the outer belt only of electrons, both being very dangerous for satellites. In order to avoid Van Allen belts, the orbit parameters of LEO and MEO satellites are chosen to surround the Earth at altitudes of 1.3–1.7 and 3.1–4.1 Earth radii. So, a typical LEO satellite has an altitude of 500–1500 km, an orbit period of 1.5–2 h, and is visible to a given Earth station for only a few

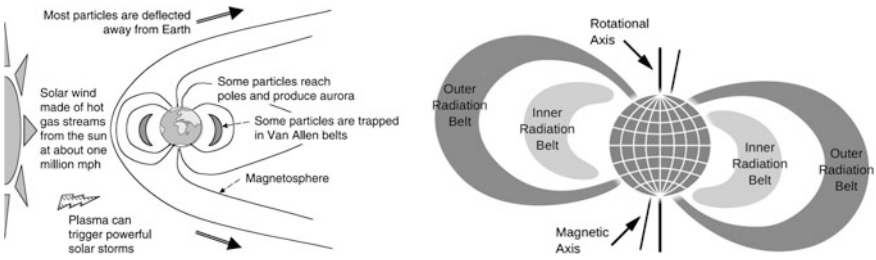

Fig. 17.2 The Van Allen Belts

minutes in every orbit period, while a typical MEO satellite is between 5000 and 12,000 km altitude with orbit period of several hours.

Today, most of the very small satellites operate in low Earth orbits (LEO), but there are no restricted orbits because of two reasons:

- mainly, their missions are usually technological demonstrations/verifications/tests/maneuvers etc. and they last as long as the communication with the Earth is maintained;
- their orbital parameters are defined at the end of the design process because of the multitude of launch possibilities, altitude and inclination flexibilities as secondary payloads.

17.1.3 Eclipses on Earth Orbits

When a satellite is on an Earth orbit (Fig. 17.3)—mostly during the equinox days when the longest eclipse appears and consists in the Earth totally blocking the solar light to illuminate the satellite—, the solar array ceases to generate the primary electrical power for the satellite and its temperature quickly falls. Therefore, for a

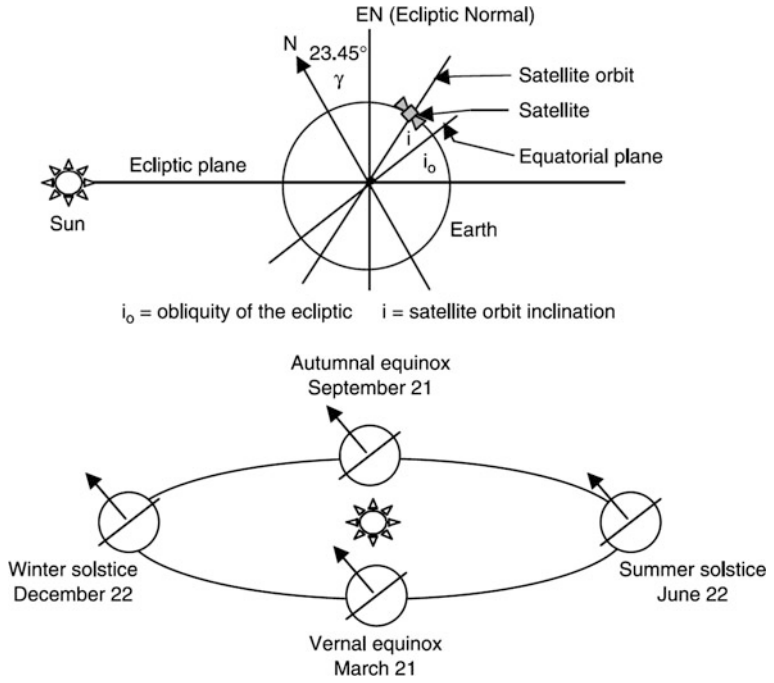

Fig. 17.3 Satellite in Earth's orbit with seasonal variations

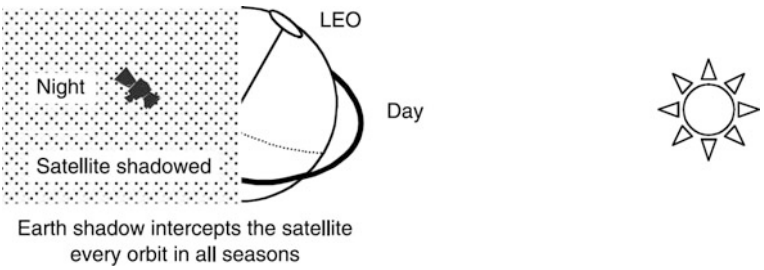

Fig. 17.4 Eclipse in near-equatorial LEO, once per orbit in all seasons

circular Earth orbit of a satellite, the eclipse duration in hours is calculated using the equation [6]:

$$T_e = \frac{1}{2} + \frac{1}{\pi} \cdot \sin^{-1} \frac{\sqrt{1 - (R_{Earth}/R_{orbit})^2}}{\cos \beta}, \tag{17.1}$$

where β is the angle of the sunlight incidence on the orbit plane that varies seasonally between ±(i + γ), i is the orbit inclination with respect to the equator and γ is the angle between the sun line and the ecliptic plane (23.45°).

Equation (17.1) above shows how the eclipse duration T_e depends on β angle: when β grows, T_e is diminished, which improves the load capability of the electrical power system. There is a specific high value of β angle when no eclipse occurs: there are polar and near-polar low Earth orbits (LEO) that never have an eclipse of the sun and $T_e = 0$. The opposite situation is when $\beta = 0$ and creates the case of the longest eclipse: in near-equatorial, circular, low Earth orbits (LEO), eclipses of approximately equal duration occur once every orbit period. As a consequence, the power system engineer starts with the orbit parameters indicated by the customer in order to obtain the orbit period, calculates the eclipse duration Te (that determines battery requirements onboard the satellite on a certain day) according to β angle.

In addition, other parameters may appear if a Moon eclipse occurs simultaneously with the Earth eclipse, when the battery must support an additional depth of discharge while temperature falls. Also, the solar flux depends of equinox and solstice and varies the power in the solar arrays with 11%. Figure 17.4 shows how the eclipse duration T_e varies with the orbit altitude, inclination, and the sunlight incidence angle on the orbit plane-in LEO, it can vary by one of two factors. All these parameters greatly affect the power system design.

17.1.4 Example of Very Small Satellites: CubeSats

A typical example of very small satellites is strongly represented today by CubeSats [9], that has been widely adopted both by universities and industry as well [10, 11]

due to many reasons distinctive from big satellites: a cheaper and faster design and launch, a larger modularization capacity by packaging many devices and sensors, project management's cost reduction, availability of the satellite's subsystems as Commercial-Off-The-Shelf (COTS) components, the control from Earth through amateur stations, simple architecture and aims etc. CubeSats are in many situations called nanosatellites, but they represent only a class of them.

The elementary cube unit of 10 cm (10 × 10 × 10 cm) and the mass smaller than 1.33 kg is known as 1U CubeSat, though even 0.5U modules are manufactured nowadays. Still, only starting from 3U CubeSat dimensions (10 × 10 × 30 cm) with a mass of 3–4 kg, small payloads can be carried in space, without mentioning the additional mandatory equipment that expands these dimensions.

CubeSats' missions are generally classified in: experimental and research missions, educational and radio amateur missions and commercial missions. As an example of the first mentioned mission, the European Space Agency (ESA) started in 2013 and will launch in 2016 (a development of 3 years) a number of four 3U CubeSats projects (GomX-3, SIMBA, QARMAN and Picasso) that are part of the QB50 flight of the In-Orbit Demonstration (IOD), which is part of the General Support Technology Programme (GSTP). Other ESA nanosatellite missions that begun in year 2014: cooperative nanosatellites (four parallel 'Sysnova' studies within the General Studies Programme), commercial telecom services nanosatellites (within ARTES 1 programme) etc. [9].

Still, there are a number of world organizations from academic and industry who design, manufacture and send in space nanosatellites whose buses comply with the requirements of a specific mission. In this case, CubeSat design specifications may be not followed.

17.2 The Electrical Power System

The electrical power system (Fig. 17.5) generates, stores, conditions, controls, and distributes power within the specified voltage band to all bus and payload equipment.

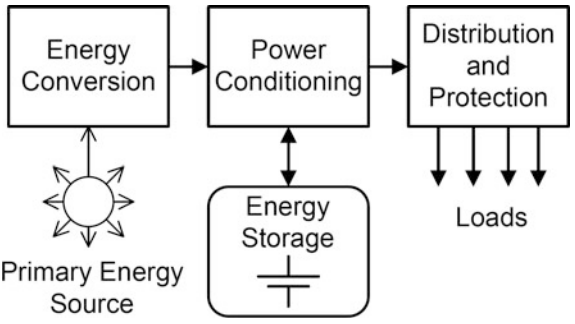

Fig. 17.5 Typical block diagram of the electrical power system

This system includes also the protection circuitry for all credible faults. For satellites that orbit Earth the primary energy source is the sun. For deep space missions, the primary energy may be supplied by other sources like the radioactive generators. The electrical energy provided by the energy conversion unit is further processed by the power conditioning unit. Power conditioning unit includes the maximum power point tracker, bus voltage regulator, battery charge and discharge regulators and additional DC–DC converters. Some energy may be stored into batteries in order to be delivered to the system during eclipses or high power demand periods. The distribution and protection unit includes the load switches, fuses, additional protection circuitry and the distribution harness. The harness consists of conducting wires and connectors that connect various components together.

17.2.1 The Array of Solar Cells

With few minor exceptions (low-cost, limited life missions that use non-rechargeable batteries as primary source) all satellites that orbit Earth use the solar energy. The solar energy is converted into electrical energy by meaning of the solar cells. The technology of solar arrays evolves continuously during years and the conversion efficiency increase significantly. Table 17.3 presents the typical solar cells and their characteristics ilicon solar cells have been used for electrical power on almost all space satellites since 1958. Their scalability, reliability, and predictability have made solar cell/arrays the prime choice for spacecraft designers. Early silicon solar cells were typically ~11% efficient, and the conversion efficiency of silicon cells currently flown varies between 12.7 and 14.8%.

Table 17.3 Solar cells for space applications and their characteristics

Parameter	Silicon	High efficiency silicon	Single-junction GaAs	Dual junction GaAs + Ge	Triple junction
STC[a] efficiency (%)	12.7–14.8	16.6	19	22	26–30
STC[a] operating Voltage (V)	0.5	0.53	0.9	2.06	2.26
Cell weight (mg/cm^2)	13–50	–	80–100	80–100	80–100
Temp coefficient (%/C) at 28C	−0.0055	–	−0.0021	–	−0.0019
Cell thickness (μ)	50–200	76	140–175	140–175	140–175
Status	Obsolete	In Use	Obsolete	Nearly Obsolete	State-of-Art

[a]Standard test conditions

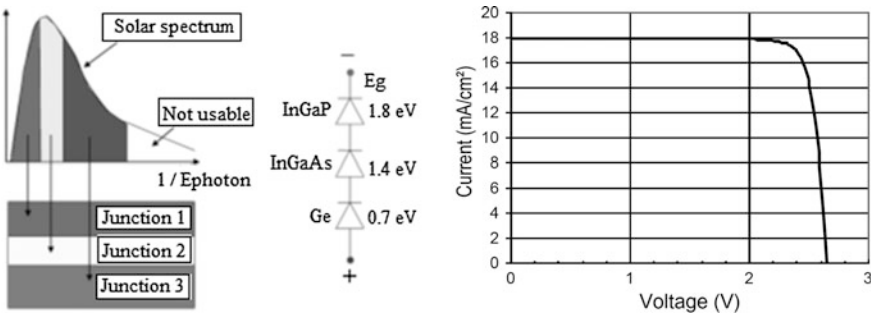

Fig. 17.6 The triple junction solar cell and the typical IV characteristic (Spectrolab)

Advanced solar cells with improved efficiency developed over the past fifteen years include: (1) single junction GaAs solar cells, (2) dual junction III-V compound semiconductor solar cells utilizing atoms from the 3rd and 5th columns of the periodic table, and (3) triple-junction III-V compound semiconductor solar cells. GaAs/Ge cells currently available on the market have an average conversion efficiency of 19% at AMO. The GaAs-type solar cells have higher radiation resistance than silicon solar cells. Dual-junction and triple-junction solar cells are presently available from several vendors. Commercially available dual-junction solar cells are 21–22% efficient.

Currently, triple-junction cells consisting of GalnP, GaAs, and Ge layers, are grown in series connected layers, and are 27% efficient in production lots [12–14]. A typical triple junction solar cell is depicted in Fig. 17.6.

17.2.2 Batteries for Space Applications

The energy storage is required to meet the spacecraft load demand not only during eclipse, but also when the demand exceeds the power generation at any time. The most widely used energy storage technology is the battery, which stores energy in an electrochemical form. There are two basic types: primary batteries (for very short duration missions) and secondary (rechargeable) batteries.

Major batteries used in the spacecraft industry at present are nickel cadmium (NiCd), nickel hydrogen (NiH2), and lithium-ion (Li-ion):

- NiCd batteries were the first type used in space applications. They have a medium energy density of about 30 Wh/l, the depth of discharge (DOD) is of 0.5%/day, and their operating temperature is from 0 up to 40 °C, offer relatively lower specific energy, is temperature sensitive, each elementary cell develops 1.2 V and has shorter cycle life. Even if SuperNiCd has better parameters, under environmental regulatory scrutiny, the cadmium has been placed, and today NiH2 has replaced the NiCd batteries for most space applications;

- NiH2 batteries were the last 20 years the main option for LEO and GEO applications because of their higher medium energy density of 60 Wh/l, having a the depth of discharge (DOD) is of 0.5%/day. Each elementary cell develops 1.2 V and the operating temperature starts at −20 °C support up to 30 °C;
- Li-ion batteries offer significantly higher specific energy density over that of NiH2 (from 150 up to 400 Wh/l) and perform better at low temperatures. Modern Li-Ion batteries can operate with good performance in a range between −40 and 65 °C. The production cost is relatively high but can be competitive with NiH_2 in the same volume production. It is vulnerable to damage under over-charging or other shortcomings in the battery management. Therefore, it requires more elaborate charging circuitry with adequate protection against over-charging [15].

17.2.3 Topologies of the Power Conditioning Unit (PCU) for Small Satellites

The three most common power system implementation approaches found on today's small satellites that are presented below are: Direct Energy Transfer (DET) with Battery Bus, DET with Regulated Bus and the Maximum Power Point Tracker with Battery Bus The following sections describe the operation of each of the above systems.

17.2.3.1 Direct Energy Transfer with Battery Bus (DET-BB)

This topology is depicted in Fig. 17.7. The DET topology offers simplicity being often selected for space missions where the mass is critical. There are no switch-mode DC–DC converters involved in this topology, a major advantage for mass (no magnetic components), reliability (no high speed power components) and EMI. There are few disadvantages associated with this topology. The battery is directly connected to the PV voltage and a larger solar panel is required in this case to ensure the proper energy transfer. A larger panel means a higher price for the mission. Also in order to avoid excessive losses due to the presence of the Shunt Regulator the voltage and operating point of panel should be well known before launching.

17.2.3.2 Direct Energy Transfer with Regulated Bus (DET-RB)

This second topology is favored by the European Space Agency (ESA) and can be found in many European spacecrafts [16]. Typical architecture of this topology is depicted in Fig. 17.8. A Sequential Switching Shunt Regulator (**S3R**) regulates the

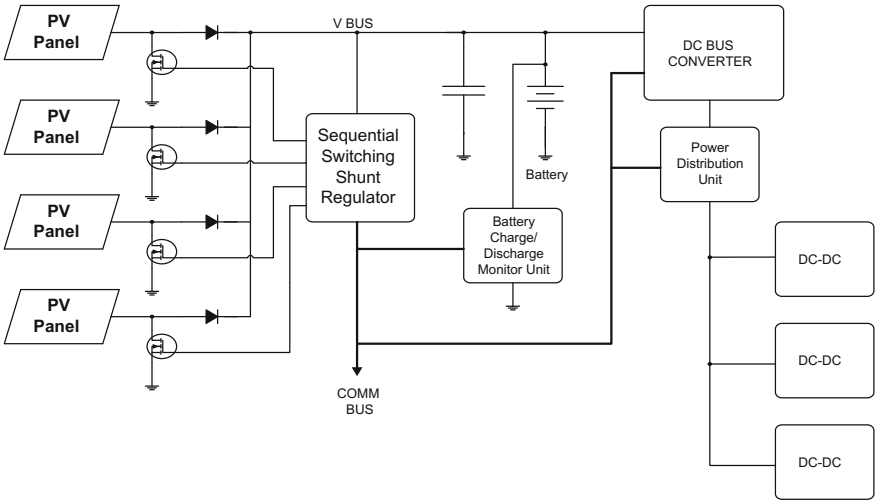

Fig. 17.7 Direct energy transfer with battery bus topology

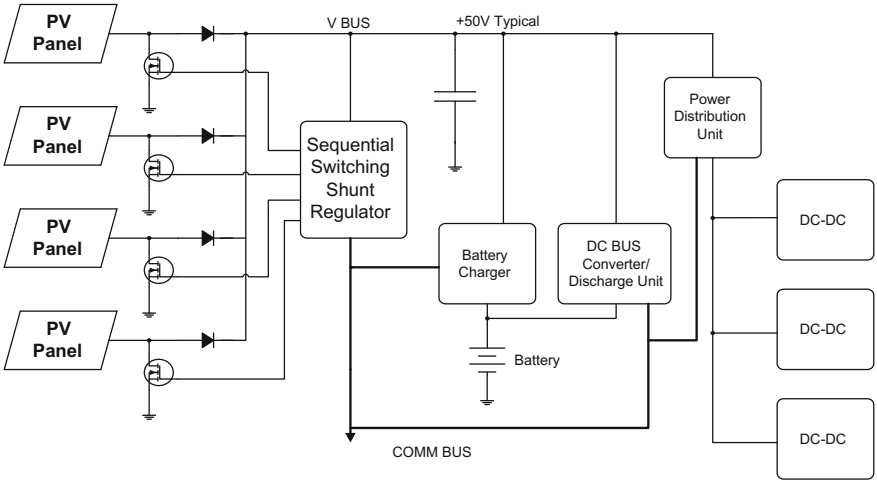

Fig. 17.8 Direct energy transfer with regulated bus

bus voltage (V BUS) to a typical value, usually between 24 and 50 V. This topology is well suited for missions where the spacecraft experiences extended periods of sunlight plus occasional long eclipse period like in case of GEO satellites.

Power flows directly from panels to the bus via the blocking diodes and is regulated by S3R regulator during sunlight period. The Battery Discharge Regulator (BDR) will keep the bus voltage within regulation limits during eclipses or periods

with high power demand. The DET-RB topology offers high efficiency for spacecrafts with medium to high power demands orbiting GEO or GTO. The solar arrays must operate at maximum power point for optimum performance of this topology. When used in LEO, this power system will require the use of solar arrays much larger than that required by an MPPT bus, but for GTO or GEO, the solar arrays can be sized for the equilibrium array temperature so that a smaller proportion of the potential array power is left in the panels.

The battery must be discharged during eclipses by BDR to a value that ensures optimum regulation of the bus voltage by S3R regulator. The BDR is usually implemented using a switch-mode DC–DC converter and this may impact the final efficiency of the system especially in case of prolonged eclipses.

This topology can be implemented using simple components like operational amplifiers and comparators already qualified for space operation, which is considered a major advantage for larger satellites at higher orbits.

17.2.3.3 Maximum Power Point Tracker with Battery Bus (MPPT-BB)

This power system architecture uses a different approach. Instead of connect directly the output of the solar array to the battery a Maximum Power Point Tracker (MPPT) is used now to process the available energy from array. During sunlight the MPPT charge the battery, supply the bus voltage and ensure that the array operates at maximum power point. The MPPT also regulates the bus voltage after the battery reaches the end of charge state, the shunt regulator being now eliminated.

A block diagram of this topology is depicted in Fig. 17.9. The MPPT is usually implemented using a switch-mode DC–DC converter and a special control loop

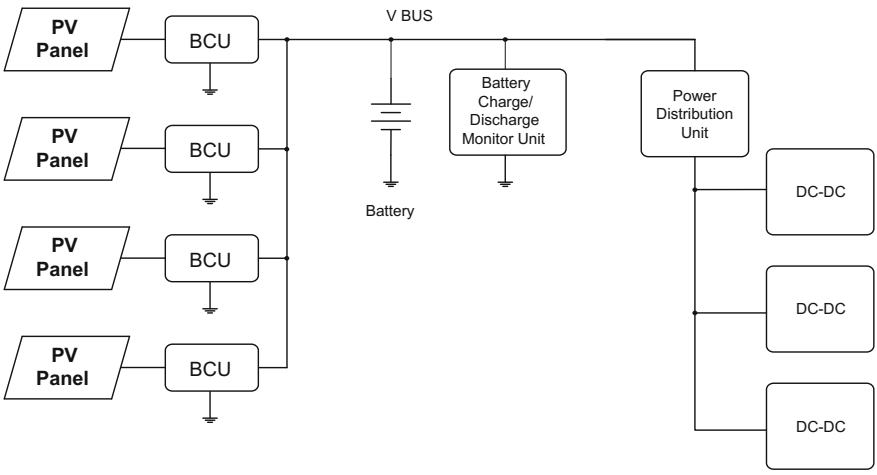

Fig. 17.9 Maximum power point tracker with battery bus

capable to track the maximum power point (MPP) of the array. The efficiency of this DC–DC converter should be as high as possible in order to minimize energy losses. A small amount of the available energy (5–10%) will be lost due to this converter. However, this architecture may achieve a better overall efficiency compared with previous topologies in case of satellites orbiting LEO where the array temperature, and hence MPP, changes considerably over the sunlight period of the orbit. This topology can be used also for small satellites without pointing gimbals where the solar array is not always oriented towards the sun. For GEO satellites where there are extended periods of sunlight and solar arrays at equilibrium temperature, the inefficiency of the MPPT would make the use of this topology impractical [11].

This topology is preferred for very small satellites like Cube Sat orbiting on LEO. The presence of the MPPT regulator increases the complexity of this topology. While the MPPT controller can be implemented in the analog domain using simple, space qualified components (operational amplifiers and comparators), the best performance of the MPPT algorithms requires digital implementation. The presence of a microcontroller or a digital signal processor (DSP) for implementing the MPPT algorithms reduces the radiation hardness of the system. This is not usually a problem for low cost LEO missions with limited life span.

17.2.4 Maximum Power Point Tracker (MPPT)

The MPPT is a common technique for terrestrial applications due to the typical output characteristic of a PV panel. The MPP of the panel depends on many factors like the irradiation and operating temperature. MPPT will ensure that the maximum available energy is processed and delivered to the load. However, for space applications this technique is in many cases avoided. For satellites orbiting high orbits the complexity associated with the implementation of MPPT is not justified. The orbit parameters are well defined before launching and the power system can be designed for optimum performance without the presence of MPPT. Here, architectures based on Direct Energy Transfer (DET) are more appropriate as the eclipse period is shorter.

In LEO, where the battery must be charged in a short period, the power point tracker (PPT) allows maximum power to be captured for several minutes after each eclipse when the array is cold. Architecture without the PPT feature, such as a direct energy transfer (DET) bus (as presented in Sects. 17.2.3.1 and 17.2.3.2), would waste a significant amount of power, as shown in Fig. 17.10. If DET systems were designed to deliver the required power at one-half the illumination at battery's end of life (EOL), the power waste would be C-D watts at EOL full sun, B-C-D watts at battery's beginning of life (BOL) full sun, and A-B-C-D watts at EOL full sun on a cold array. The PPT design eliminates this waste by utilizing all the power that can be generated.

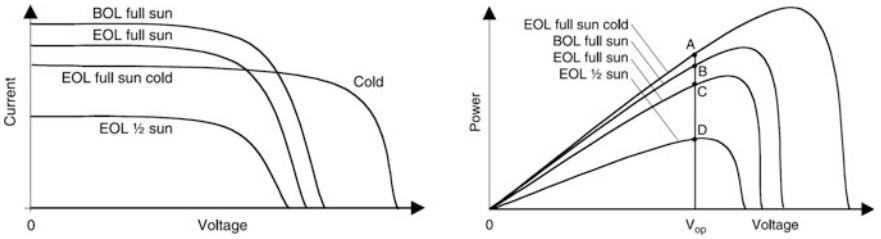

Fig. 17.10 Power wasted in direct energy transfer architecture in certain conditions

The main advantages of the peak power tracking are that it maximizes the solar array output power all the time, and it does not require the shunt regulator and the battery charge regulator. On the other hand, the MPPT requires a DC–DC converter and there are losses associated with this converter that may affect the efficiency of the power system. Moreover, since this loss is dissipated inside the spacecraft body, it negatively impacts the thermal system. For very small satellites orbiting LEO the power system based on MPPT brings real advantages. This system will maximize the utilization of PV panels and due to low energy requirement of these satellites, the additional DC–DC converter losses will not significantly affect the thermal system.

17.2.4.1 The Model of the Solar Cell

A photovoltaic (PV) cell is basically a large photodiode that will convert the incident solar energy to electricity based on the well-known photovoltaic effect. The electrical equivalent model of a PV cell is depicted in Fig. 17.11.

A PV panel is made from n identical cells connected in series, like in Fig. 17.12. The current source in Fig. 17.11, i_{sun}, is proportional to the amount of irradiation, and linear with respect to the PV cell temperature. The current is given by:

$$i_{sun} = \left(i_{sun,STC} + k_{temp} * (T_{cell} - T_{cell,STC})\right) * \frac{P_{sun}}{P_{sun,STC}} \tag{17.2}$$

where i_{sun} and $i_{sun,STC}$ is the short circuit current at the given working point and standard test conditions (STC), respectively. The constant k_{temp} is the temperature

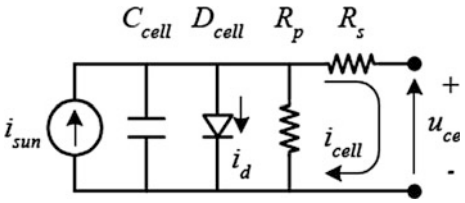

Fig. 17.11 PV cell equivalent model

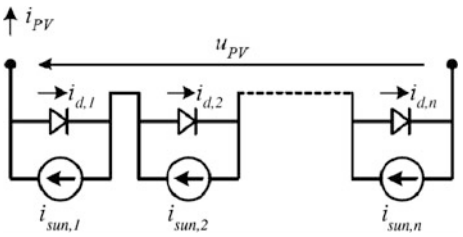

Fig. 17.12 PV panel schematic

coefficient of i_{sun}. T_{cell} and $T_{cell,\ STC}$ are the actual and STC cell temperatures, respectively. Finally, P_{sun} and $P_{sun,STC}$ are the irradiations at the present operating point and at STC, respectively [17]. The current through the diode is expressed by:

$$i_d = i_S * \left(e^{\frac{q*u_d}{k*A*T_{cell}}} - 1\right) \tag{17.3}$$

where i_S is the reverse saturation current, A is the diode idealization factor (usually defined between 1 and 5), and u_d is the voltage across the diode. The PV cell equivalent model contains some additional elements, R_p and R_s. These circuit elements are associated with parasitic like the connection wires between cells. A more detailed description of these parasitic elements is found in [12, 13]. The C_{cell} is the capacity associated with the pn junction of the diode. Finally, the current, voltage and power generated by a single PV cell are expressed by:

$$i_{cell} = i_{sun} - i_d \tag{17.4}$$

$$u_d = u_{cell} + R_s * i_{cell} \tag{17.5}$$

$$P_{cell} = u_{cell} * i_{cell} \tag{17.6}$$

A family of curves that plot the i_{cell} and u_{cell} versus the irradiation is depicted in Fig. 17.13. The power delivered by the PV cell under different irradiation conditions is depicted in Fig. 17.14 [18].

The power delivered by the PV cell has a maximum at certain voltage and this maximum depends on the irradiation. In order to extract the maximum available power delivered by the PV panel in certain illumination conditions, a certain techniques must be implemented in the system that process the photovoltaic energy.

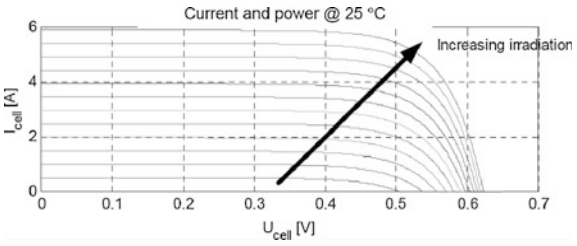

Fig. 17.13 I_{cell} and U_{cell} versus irradiation

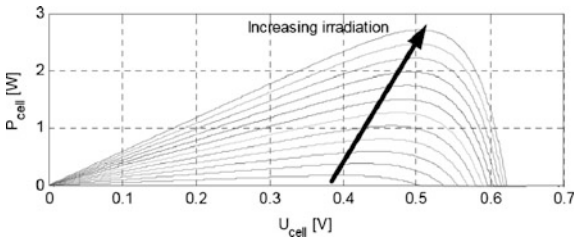

Fig. 17.14 P_{cell} and U_{cell} versus irradiation

17.2.4.2 Algorithms for the MPPT

There are many MPPT algorithms developed during years. Table 17.4 summarize the available algorithms and presents their important features and characteristics [19, 20]. Simple algorithms like Hill-climbing/Perturb&Observe gain popularity over years due to simplicity but suffer from certain drawbacks like inability to distinguish between a local and absolute power maximum. The scientific community concentrates the efforts to solve various drawbacks associated with simple algorithms and finally the complexity of the MPPT grows exponentially. The MPPT algorithms become more robust but the complexity and cost of the implementation increases substantially. However, for space applications main criteria are reliability and simplicity. The MPPT should be able to continuously track the true MPP in minimum amount of time and should not require periodic tuning. In this case, hill climbing/P&O, fractional V_{OC} or I_{SC} with their low implementation complexity are appropriate.

The Fractional Open-Circuit Voltage Algorithm

This algorithm is based on the observation that the MPP voltage is a fraction of the open voltage of the solar panel.

$$U_{MPP} = K * U_{OC} \tag{17.7}$$

where: U_{MPP}—MPP voltage, U_{OC}—open circuit voltage, K—a constant (usual between 0.7 and 0.85 for silicon cells).

The implementation of this algorithm is depicted in Fig. 17.15. A switch disconnects momentarily the panes from the load and the MPPT bloc measure the open circuit voltage of the PV panel. The MPP voltage is estimated using (17.7). This simple algorithm requires only one sensor for implementation (voltage sensor). The associated are:

- relative low efficiency of MPPT due to the fact that the K constant cannot be very precise determined.
- when the panel is disconnect from the load, no power flows for a short period of time. This may decrease the efficiency of the system.

Table 17.4 Major MPPT techniques and their salient characteristics

MPPT technique	PV array dependent?	True MPPT?	Analog or digital?	Periodic tuning?	Convergence speed	Implementation complexity	Sensed parameters
Hill-climbing/P&O	No	Yes	Both	No	Varies	Low	Voltage, current
IncCond	No	Yes	Digital	No	Varies	Medium	Voltage, current
Fractional V_{OC}	Yes	No	Both	Yes	Medium	Low	Voltage
Fractional I_{SC}	Yes	No	Both	Yes	Medium	Medium	Current
Fuzzy logic control	Yes	Yes	Digital	Yes	Fast	High	Varies
Neural network	Yes	Yes	Digital	Yes	Fast	High	Varies
RCC	No	Yes	Analog	No	Fast	Low	Voltage, current
Current sweep	Yes	Yes	Digital	Yes	Slow	High	Voltage, current
DC link capacitor droop control	No	No	Both	No	Medium	Low	Voltage
Load *I* or *V* Maximization	No	No	Analog	No	Fast	Low	Voltage, current
dP/*dV* or *dP*/*dI* feedback control	No	Yes	Digital	No	Fast	Medium	Voltage, current
Array reconfiguration	Yes	No	Digital	Yes	Slow	High	Voltage, current
Linear current control	Yes	No	Digital	Yes	Fast	Medium	Irradiance
I_{MPP} & V_{MPP} computation	Yes	Yes	Digital	Yes	N/A	Medium	Irradiance. Temperature
State-based MPPT	Yes	Yes	Both	Yes	Fast	High	Voltage. Current
OCC MPPT	Yes	No	Both	Yes	Fast	Medium	Current
BFV	Yes	No	Both	Yes	N/A	Low	None
LRCM	Yes	No	Digital	No	N/A	High	Voltage. Current
Slide control	No	Yes	Digital	No	Fast	Medium	Voltage, Current

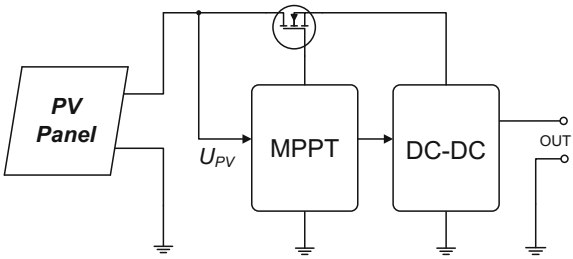

Fig. 17.15 Implementation of the "Fractional open-circuit voltage algorithm"

The inherent low complexity makes this algorithm a potential candidate for space applications. The algorithm can be implemented using only analog components, a significant advantage for space applications. However, the presence of a microcontroller will increase the flexibility of the MPPT system.

A simplified version of this algorithm is usually implemented in commercial integrated circuits. In this simplified implementation, the MPP voltage is set to a fix value by the circuitry and the panel is not disconnected from the load. The MPP voltage can be determined from the datasheet of the PV panel or by measurements.

For very small satellites where the orbit parameters are known this algorithm may be a good option. However, the orbit parameters are usually not well defined before launching for most very small satellites.

The Fractional Short-Circuit Current Algorithm

This algorithm is similar with the previous one and is based on the observation that the maximum delivered current for a panel is a fraction of the short-circuit current.

$$I_{MPP} = K*I_{SC} \tag{17.8}$$

where: I_{MPP}—current at MPP, I_{SC}—short-circuit current, K—a constant (usual between 0.7 and 0.85 for silicon). The implementation of this algorithm is depicted in Fig. 17.16.

A switch short circuit momentarily the output of the PV panel and the short-circuit current is measured by the MPPT block. The optimum output current of panel is determined with Eq. (17.8).

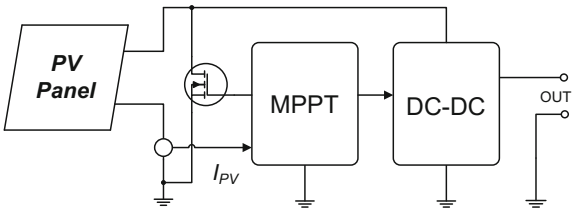

Fig. 17.16 Implementation of the "Fractional short-circuit current algorithm"

The advantages and disadvantages of this algorithm are similar with the fractional open circuit voltage algorithm. Some topologies of power converters, where the main switch is referred to ground like boost and SEPIC, can be used for implementation of this algorithm. In this case, the main switch of the converter is also used as short-circuit switch for the PV panel.

The Perturb and Observe Algorithm

This algorithm is probably the most used for MPPT systems (Fig. 17.17). The main advantage of this algorithm is his inherent insensitivity to PV panel parameters and operating conditions. The P&O is a high performance algorithm capable to find and track the MPP with greater accuracy. This algorithm perturbs the operating point of the PV panel and monitors the effects of this perturbation on the output power. If the power increases, the perturbation should be kept in the same direction; otherwise, it should be reversed [21].

In order to implement this algorithm, two parameters of the PV panel must be measured: the output voltage and the output current. The presence of two sensors increases the complexity of the MPPT system (Fig. 17.18).

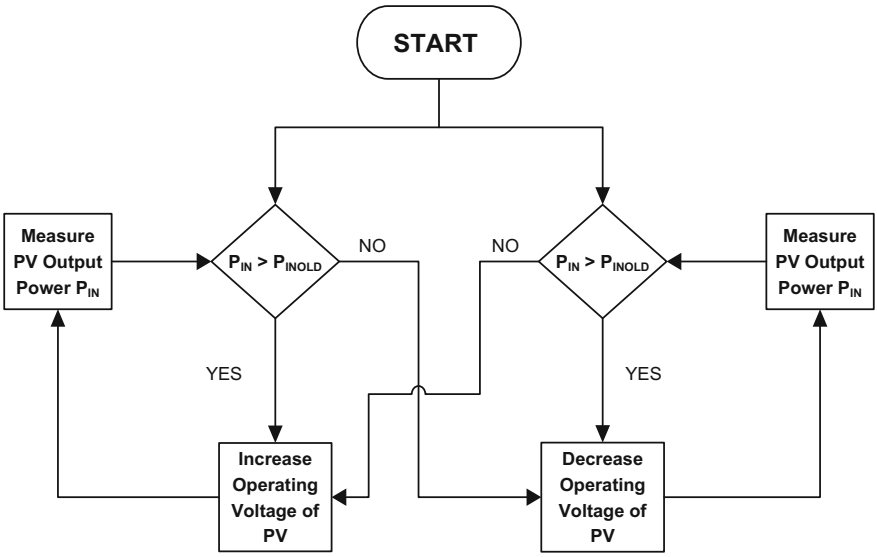

Fig. 17.17 Logic diagram of P&O algorithm

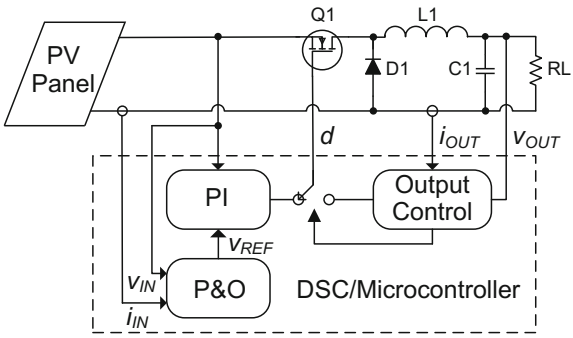

Fig. 17.18 Implementation of P&O algorithm using a DSC or microcontroller

17.3 A Flexible Architecture of Power Conditioning Unit (PCU) for Very Small Satellites

A flexible, scalable architecture for Power Conditioning Unit (PDU) of very small satellites is presented in Fig. 17.19. This architecture can be used for nanosatellites and picosatellites on LEO with maximum power requirement up to 50 W. The architecture contains the following functional blocks:

- the Chargers Unit (CU)—this unit is responsible for processing the power available from the PV panels.
- the Battery Unit (BU)—this unit contains the main battery of the PCU and the associated monitoring electronics (The Battery Charge/Discharge Monitor Unit (BCDMU)).
- the Isolation Unit (IU)—this unit provides galvanic isolation between the main battery unit and the rest of the PCU, a requirement for some missions. This unit is optional and can be removed if the mission does not require a galvanic isolation.
- the Point-of-Load/Distribution Unit (POL/D). This unit contains the Point-of-Load converters and the distribution switches. This unit includes a variable number of converters that produces the required voltages.

This architecture is well suited for satellites that orbits LEO, where the number of eclipses is high and the solar panels experience large temperature variations. The system provides the required redundancy for certain satellites as well as some advanced features that can be usually found in larger satellites like galvanic isolation. Each functional subsystem is independent and can be used as a standalone building block for simple or more complex applications. For example, the BCU unit can be used as a standalone battery charging block for low cost missions, where the space and weight is a premium.

The BCU unit implements a high performance MPPT algorithm and this is an important advantage especially for very low cost missions where the orbit can be changed just before or during launching and reprogramming of the energy

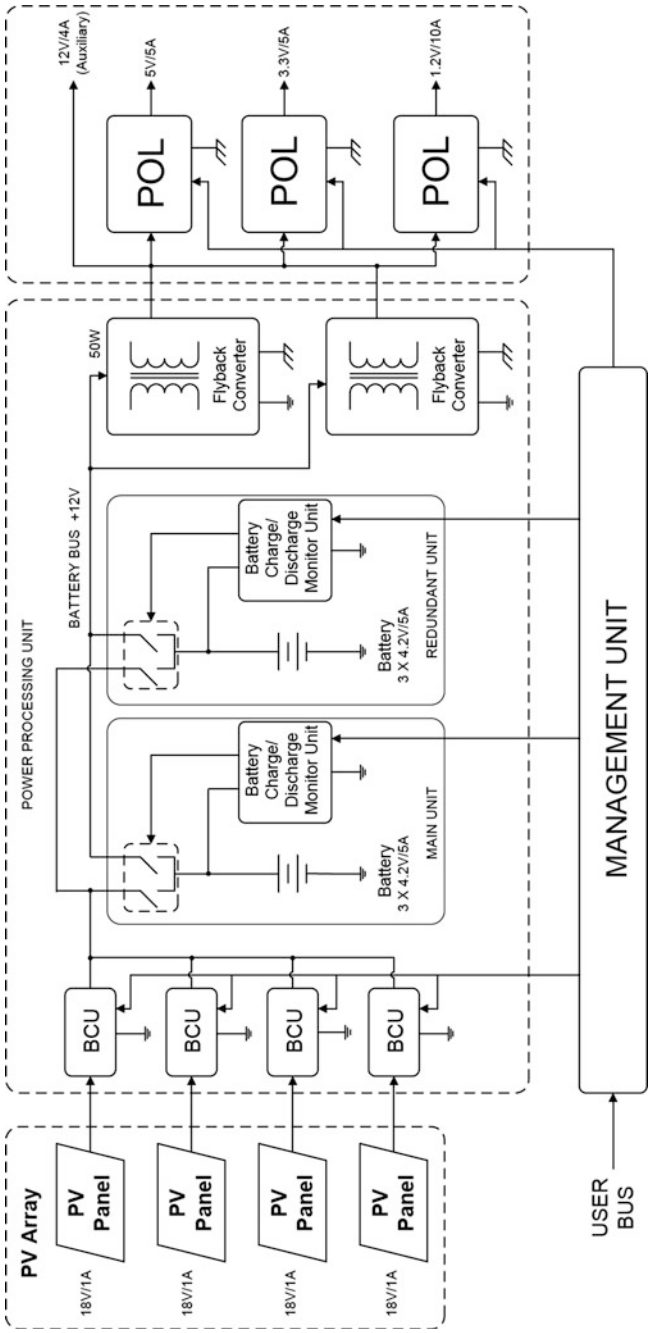

Fig. 17.19 Flexible architecture for power conditioning unit

processing unit is basically impossible or very difficult. The isolation unit and the POL units are implemented using planar magnetics in order to achieve best performance and high power density.

17.3.1 The Battery Charger Unit (BCU)

The Battery Charger Unit (BCU) is the frontend of the proposed architecture. The MPPT and battery charger algorithms are implemented by this unit (Fig. 17.20).

Due to the physical dimensions constraints, this board uses fully digital control. Digital control offers increased flexibility as most of the control parameters can be now adjusted by firmware. The BCU has two functional subunits:

- the DC–DC Power Converter, responsible with the energy conversion.
- the Digital Controller, responsible with the implementation of the MPPT algorithm, battery charging algorithm and power converter control.

The measured parameters are: the input voltage (panel voltage), the input current (panel current) and the output voltage (battery voltage). The input voltage and current are used for the MPPT algorithm implementation, while the output voltage is regulated as part of the battery charging algorithm.

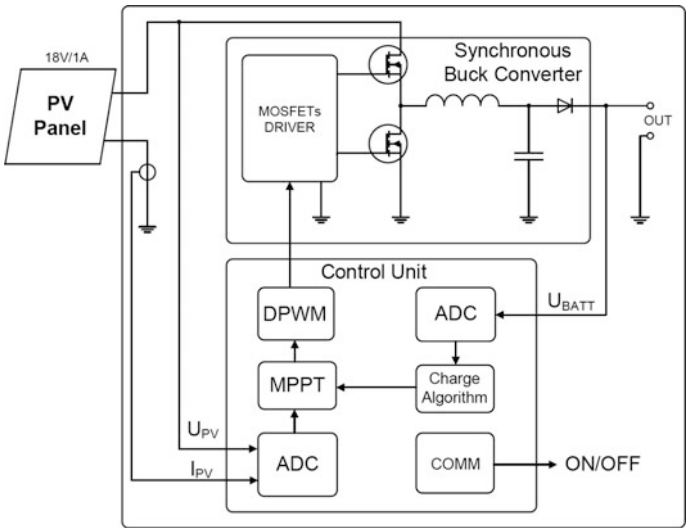

Fig. 17.20 Bloc diagram of the BCU unit

17.3.1.1 The DC–DC Power Converter

The DC–DC power converter uses the synchronous buck converter topology [22]. This topology offers high conversion efficiency and a good controllability. The output voltage is always lower than the input voltage, this topology being recommended for satellites with larger solar panels like the 2U and 3U CubeSats. For satellite with small solar panels like 1U CubeSat, the topology must offer boost or buck-boost capability. Such topologies are boost and Single-Ended Primary Inductor Converter (SEPIC) [23].

The power train of the synchronous buck converter is represented in Fig. 17.21. The freewheeling diode D is replaced by a synchronously-controlled switch Q2. In this case the losses associated with voltage drop on D are greatly reduced, a significant advantage for high output current converters.

The design entry parameters are summarized in Table 17.5. The BCU accepts 7 to 24 V at input. The output voltage is adjustable between 4.2 V (floating voltage for a single cell Li-Ion battery) to 16.8 V (floating voltage of four cells Li-Ion battery). The maximum output current is 1.75 A and is adjustable from firmware. The switching frequency is fixed, 62.5 kHz but the microcontroller has the option to internally adjust this frequency if dithering is required.

The typical design equations for synchronous buck converter are summarized in Table 17.6.

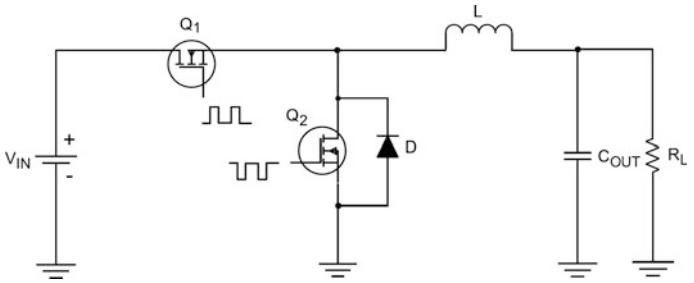

Fig. 17.21 The synchronous buck converter

Table 17.5 Design entry parameters for synchronous buck converter

Input voltage range	7–24	V
Output voltage range	4–18	V
Maximum input current	1.5	A
Maximum output current	1.75	A
Maximum output power	15	W
Input voltage ripple	≤ 500	mVpp
Output voltage ripple	≤ 150	mVpp
Switching frequency	62.5	kHz
Target efficiency	≥ 90	%

Table 17.6 Design equations for synchronous buck converter

Inductor value (H)	$L = (V_{IN_{MAX}} - V_{OUT}) * \frac{V_{OUT}}{V_{IN_{MAX}}} * \frac{1}{f_{SW}} * \frac{1}{0.5 \times I_{OUT_{MAX}}}$
Inductor peak current (A)	$I_{L_{PEAK}} = I_{OUT_{MAX}} + \frac{0.5 * I_{OUT_{MAX}}}{2}$
Inductor RMS current (A)	$I_{L_{RMS}} = \sqrt{I_{OUT}^2 + \frac{I_{Ripple}^2}{3}}$
Minimum capacitance for input capacitor (F)	$C_{IN_{MIN}} = \frac{I_{OUT} * D * (1-D)}{f_{SW} * (V_{Ripple} - D * I_{OUT} * ESR)}$
RMS current in the input capacitor (A)	$I_{RMS(C_{IN})} = \left(I_{OUT} + \frac{I_{Ripple}}{12}\right)\sqrt{D} - \frac{V_{OUT} * I_{OUT}}{V_{IN}}$
Output voltage ripple (V)	$V_{Ripple} = I_{Ripple} * \left(ESR + \frac{1}{8 * C_{Out} * f_{SW}}\right)$
RMS value for high-side current (A)	$I_{RMSHigh-Side} = \sqrt{D * \left(I_{OUT}^2 + \frac{I_{Ripple}^2}{12}\right)}$
Conduction losses for high-side MOSFET (W)	$P_{CONDHigh-Side} = I_{RMSHigh-Side}^2 * R_{DS(on)HS(max)}$
Switching losses for high-side MOSFET (W)	$P_{SWHigh-Side} = \left(\frac{V_{IN} * I_{OUT}}{2}\right) * \left(t_{s(HL)} + t_{s(LH)}\right) * f_{SW}$
Total power losses for high-side MOSFET (W)	$P_{LossHigh-Side} = P_{CONDHigh-Side} + P_{SWHigh-Side}$
RMS current for low-side MOSFET (W)	$I_{RMSLow-Side} = \sqrt{(1-D) * \left(I_{OUT}^2 + \frac{I_{Ripple}^2}{12}\right)}$
Conduction losses for low-side MOSFET (W)	$P_{CONDLow-Side} = I_{RMSLow-Side}^2 * R_{DS(on)LS(max)}$
Body diode conduction losses (W)	$P_{LossBD} = I_{OUT} * V_F * t_{BD} * f_{SW}$
Body diode reverse recovery losses (W)	$P_{RR} = \frac{Q_{RR} * V_{IN} * f_{SW}}{2}$
Total power losses for low-side MOSFET (W)	$P_{Loss} = P_{CONDLow-Side} + P_{LossBD} + P_{RR}$
Controller losses (W)	$P_{loss} = V_{in}(0.005 + F_s(Q_{gate,low} + Q_{gate,high})$
Inductor losses (W)	$P_{loss} = DCR_L * I_{L,RMS}$
Output capacitor losses (W)	$P_{loss} = ESR_{Cout} * \sqrt{\frac{(0.3 * I_{out})^2}{3}}^2$
Input capacitor losses (W)	$P_{loss} = ESR_{Cin} * \left(I_{rms.high} - \frac{V_{out} * I_{out}}{V_{in}}\right)^2$
Bootstrap capacitor (F)	$C_{BOOT} = \frac{Q_{G(Total)}}{\Delta V_{DROOP}}$

A SIMPLIS model is developed and presented in Fig. 17.22, where: f_{SW}—switching frequency [Hz], I_{OUTMAX}—maximum output current [A], D—duty cycle, I_{RIPPLE}—inductor's current ripple [A]. The SIMPLIS™ small signal model of the synchronous buck converter and the associated Bode plots are presented in Fig. 17.23.

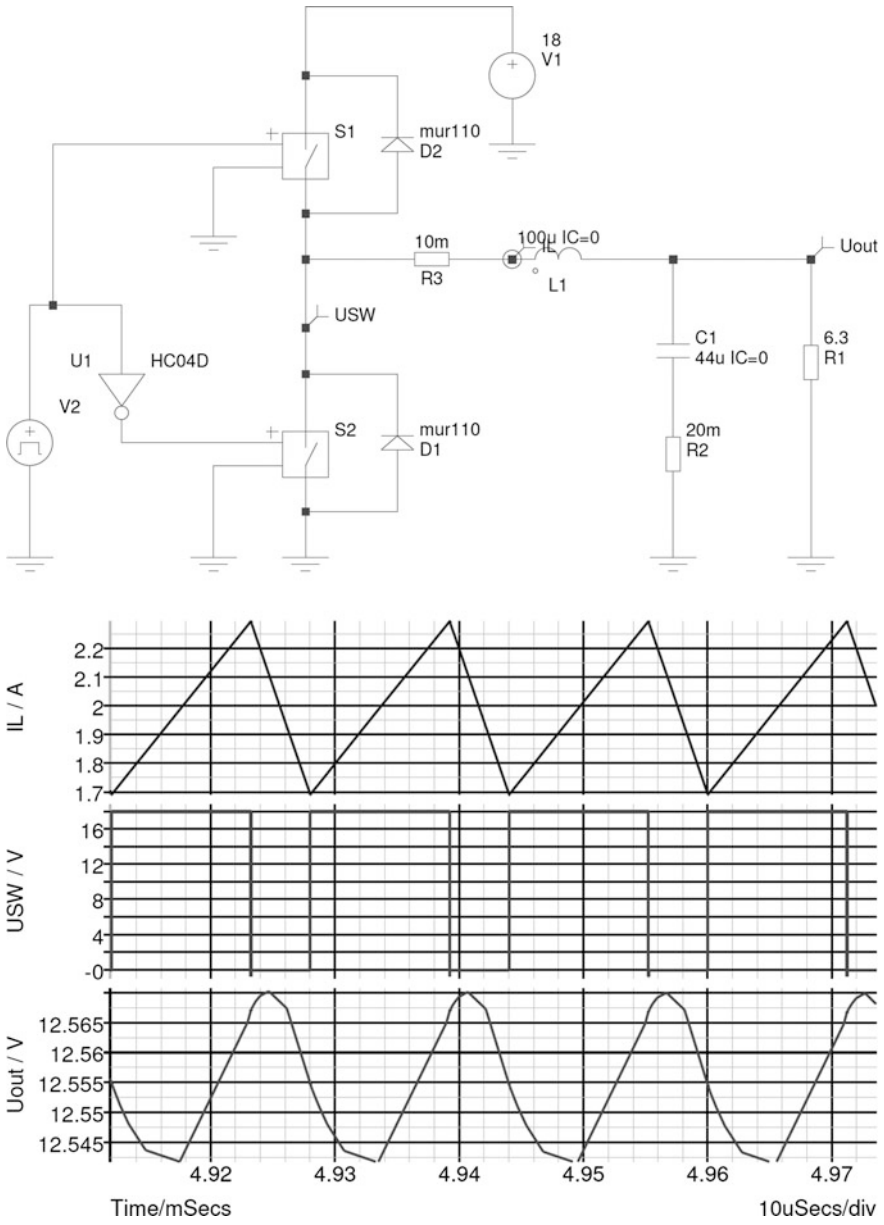

Fig. 17.22 The SIMPLISTM model of the proposed synchronous buck converter and associated waveforms of synchronous buck converter

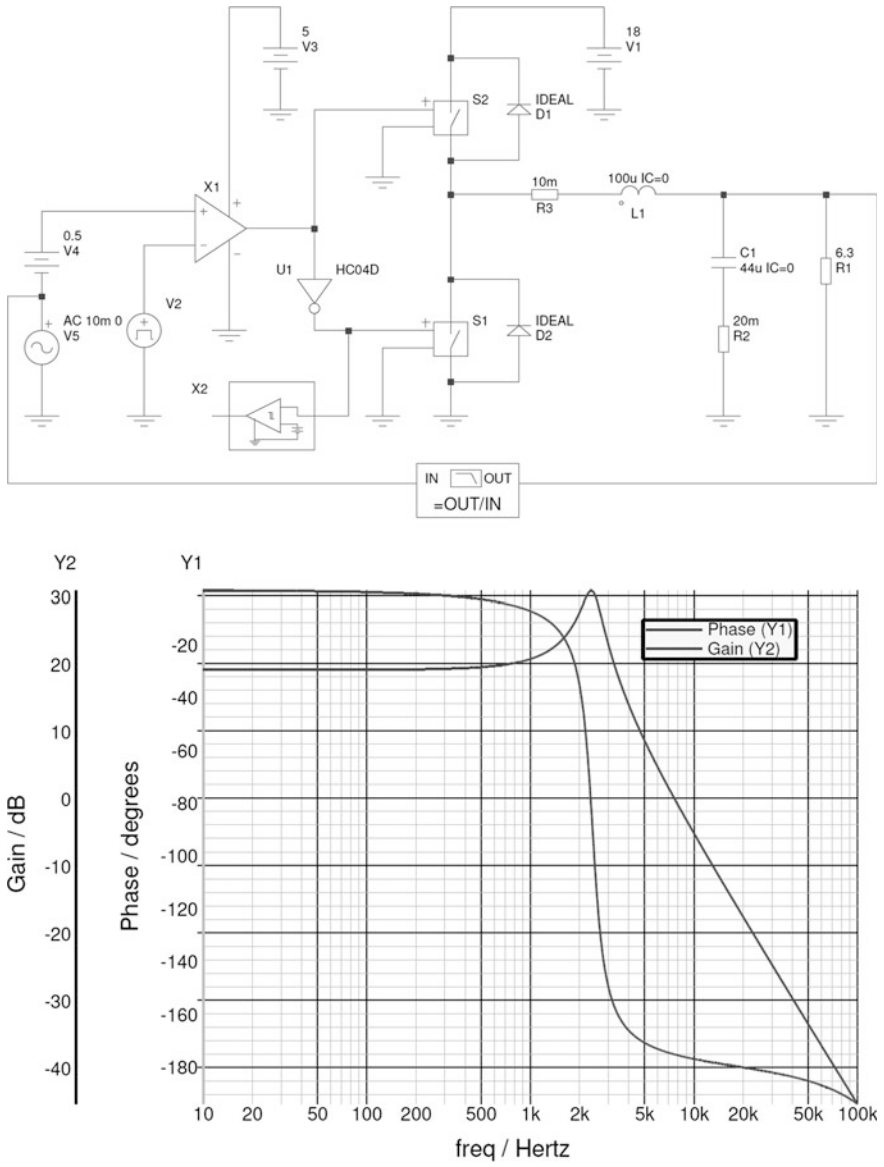

Fig. 17.23 SIMPLISTM small signal model of synchronous buck converter and the associated Bode plots

A double pole is introduced at the resonant frequency by the output LC filter. Phase sharply decrease to −180° after the resonant frequency point. There is a gain associated with the analog PWM modulator which can be calculated with:

$$G_{PWM} = \frac{V_{IN}}{V_{RAMP}} \tag{17.9}$$

where V_{IN} is the input voltage and V_{RAMP} is the amplitude of the ramp signal used to generate the PWM signal. For digital control systems the PWM modulator gain is set to 0 dB.

The synchronous buck converter requires a specialized driver circuit for MOSFETs. In case of the proposed prototype, the MOSFETs drivers are integrated into a specialized circuit, the MCP14628. This circuit is specifically designed for driving the power MOSFETs of a synchronous buck converter.

Figure 17.24 presents the internal simplified diagram of this part. This circuit is packaged in an 8-pin SOIC package and operates up to 125 °C ambient temperature. The MCP14628 driver offers also the diode emulation feature. A specific internal circuitry automatically adjust the "dead time" in order to prevent the cross-conduction phenomenon that can occurs if the "dead time" is missing or is too small.

Notable advantages of the buck converter are:

- the output voltage has a low ripple/noise, a consequence of the continuous output current of the buck converter. This is a significant advantage if the switching frequency is relatively low like in case of converters controlled by low cost digital systems.
- the buck converter running in continuous current mode (CCM) has a linear DC conversion ratio (M) equal with D (the duty cycle). This is a significant advantage if the converter is controlled by low cost digital microcontrollers with limited PWM resolution.

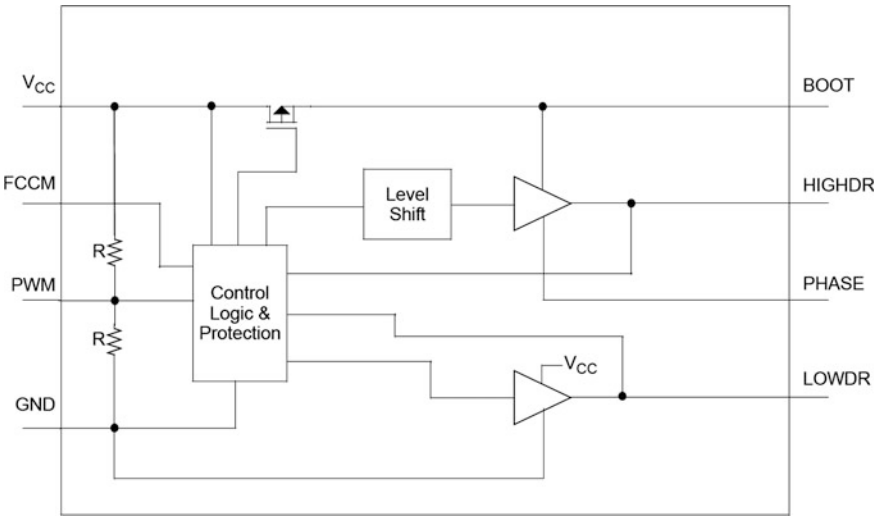

Fig. 17.24 The internal simplified diagram of MCP14628 and the package

- the buck converter has simple small signal model and is very well suited for digital control. The non-linear control techniques can be also easily implemented for this topology. The dynamic response of buck converter is excellent being the most used topology for high performance DC–DC converters.

The disadvantages of the buck converter are:

- the input current is discontinuous, creating high ripple/noise on the input voltage. The electrical stress on the input filter capacitor is high.
- the output voltage is always lower than the input voltage. This may limit the usability of this topology for certain applications.
- the buck converter requires a high-side switch driver. This increases the complexity and the cost of the schematic. Additionally, the implementation of the programmed current mode control (like the peak current mode control) is difficult due to the presence of a high-side current sensor. All these problems are solved by using monolithic integrated circuits already available from many IC producers. However, in this case the flexibility of the system may decrease and some advance control (like the implementation of the MPPT) becomes difficult to be implemented.

The buck converter is well suited for space applications either with analog or digital control. The only mandatory requirement is that the input voltage (the PV panel voltage in this case) should be always higher that the output voltage (the battery voltage in case of the proposed prototype).

17.3.1.2 The Digital Controller

The digital control of BCU is implemented using a commercial, low pin count microcontroller PIC12F1822 developed by Microchip Inc (Fig. 17.25). This microcontroller is packaged in an 8-pin package and includes all necessary blocks/features to develop a power converter:

- 10-bit Analog-to-Digital converter with up to four inputs selectable by an analog multiplexer
- digital PWM generator with up to 10-bit resolution
- low power consumption and advanced power management modes
- 8 MIPS core computational power
- internal reference voltage generator
- extended temperature operating range −40–125 °C

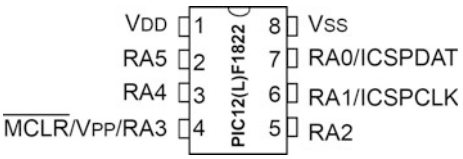

Fig. 17.25 PIC12F1822 microcontroller and the firmware flowchart

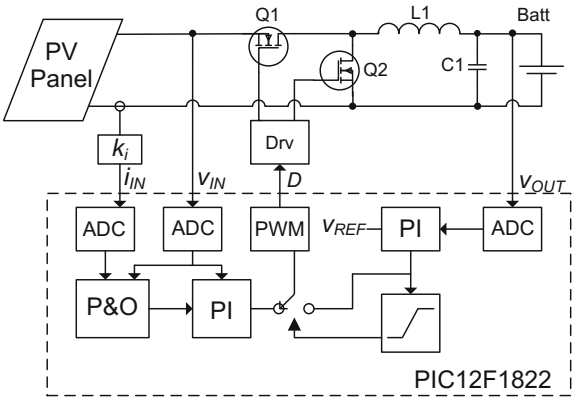

Fig. 17.26 Implementation of the BCU using PIC12F1822

The MPPT algorithm implemented in BCU is P&O and the typical block diagram of the system is depicted in Fig. 17.26. There are two PI controllers, one for the P&O algorithm and one that controls the output voltage. This architecture prevents the negative effects introduced by the transitions between operating modes of the converter (continuous conduction mode CCM and discontinuous conduction mode DCM) over the functionality of the P&O algorithm.

The firmware flowchart is presented in Fig. 17.27. Timer T1 interrupt is used for measure the required parameters. The P&O state machine runs inside the main loop and is triggered by the Measurements_Done flag set inside T1 interrupt after the completion of the measurements. The PI controllers are run inside the T1 interrupt and the update of the PWM duty cycle is done also here. The specific charging algorithm and protection state machine runs in the main loop.

The measured parameters are: the input current, the input voltage and the output voltage. The output current, necessary for chemistry-specific charging algorithm is estimated from the input power. The decision between the two operating modes, tracking and regulating, were taking based on the output of the voltage PI anti-windup comparator. If the output voltage PI controller is saturated, the system is in tracking mode and the P&O loop is executed every 15 ms. The PI controllers run simultaneous at 8 kHz.

The difference equation for each PI controller is (17.10). This equation is tailored to be implemented using only shifting operations, a significant advantage for low computational power microcontrollers:

$$y(T) = 2^m\,(y(T-1) + 2^n\ e(T) + 2^k\ e(T-1)) \tag{17.10}$$

where: e(T) = Vout(T) − Vref, m, n, k—real integers, y(n)—output of PI controller.

This simplified implementation of the PI controller may introduce additional constraints for the controlled system. The corresponding s-domain equation is:

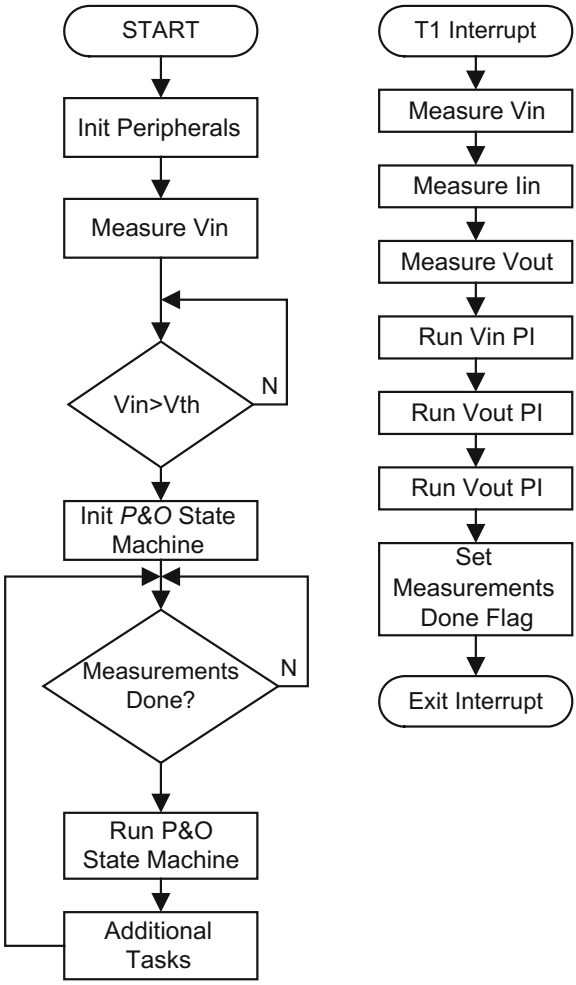

Fig. 17.27 The firmware flowchart

$$Y(s) = \frac{0.5s - 6.485E - 13}{s} \tag{17.11}$$

In this case m = 0.5, n = 0 and k = 0.

The Bode plots of the compensated system are represented in Fig. 17.28. The system using this simplified control has a slow response but the phase and gain margins are good. The slow response of the system is not a problem as the load is a battery and the input voltage has also a slow variation. Some adjustments of the system phase and gain margins can be done by slightly adjusting the value of the inductor and/or the value of the output capacitor.

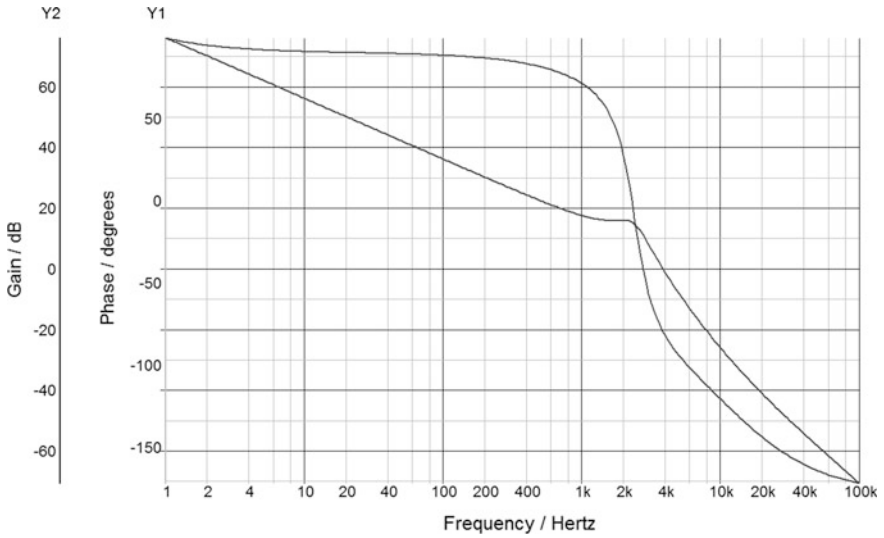

Fig. 17.28 Bode plots of the compensated system

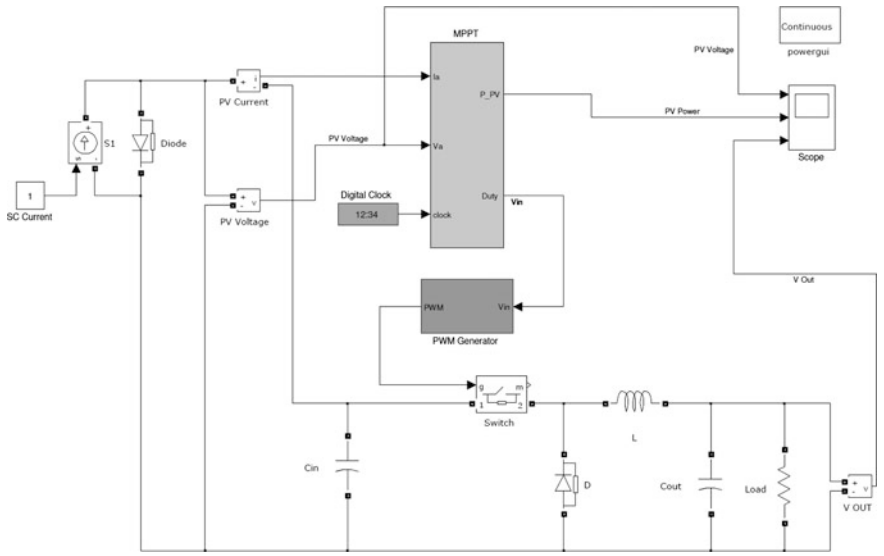

Fig. 17.29 The SimulinkTM model of the system

A Simulink™ model of the P&O algorithm implemented using a buck converter is presented in Fig. 17.29. The perturbation step is set to 1%. In this case the MPP voltage and current of the panel are of 10 V and 1 A, so that the MPP power is 10 W (Fig. 17.30).

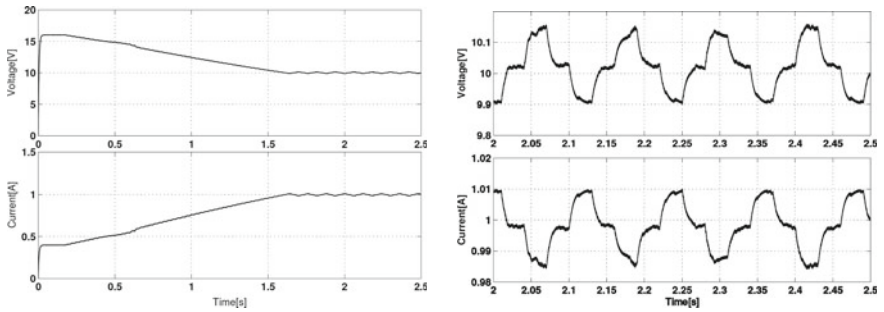

(a) PV vol voltage and current during locking phase

(b) PV voltage and current during steady state

Fig. 17.30 PV voltage and current during locking phase and during steady state

17.3.1.3 The BCU Sensors Circuitry

The BCU unit monitors three parameters: input voltage (panel voltage), input current (panel current) and the output voltage (battery voltage). The input voltage and the input current are used for the implementation of the MPPT algorithm and the output voltage is used for the implementation of the battery-specific charging algorithm.

The input voltage is measured using a voltage divider. The ratio of this divider should be adjusted according with the input voltage range in order to maximize the dynamic range of the input voltage measurement circuitry. For the input voltage range between 9 and 24 V the divider ration is set to 4.7 (100 K with 27 K). A small capacitor is placed in parallel with the low-side resistor in order to form a low-pass filter that cleans the output of the voltage divider.

The input current is measured using a 0.1 Ω low-side shunt placed in series with the "Negative" terminal. An inverting amplifier is used to amplify the voltage drop across the shunt and to restore the correct polarity of the current sense signal. The gain of this amplifier should be adjusted according with the hardware requirements in order to maximize the dynamic range of the current sense circuitry. For the proposed prototype, the gain of this amplifier is set to −20X resulting in a conversion gain of the current sense circuitry of 2 V/A. A snapshot of the input current sense amplifier and the output voltage sense buffer circuits are presented in Fig. 17.31. The response of the sense amplifier is set to be of a low-pass filter (with pole introduced by C9) in order to provide a clean output signal and reject the noise introduced by the switch-mode power converter. The circuit is built around MCP6022 dual operational amplifier. The bandwidth of this operational amplifier is 10 MHz and the maximum operating ambient temperature is 125 °C.

The output voltage is measured using a voltage divider. Because this divider is always connected across the battery voltage and because up to four charger units can be connected in parallel in the same time, the values of the resistors are very

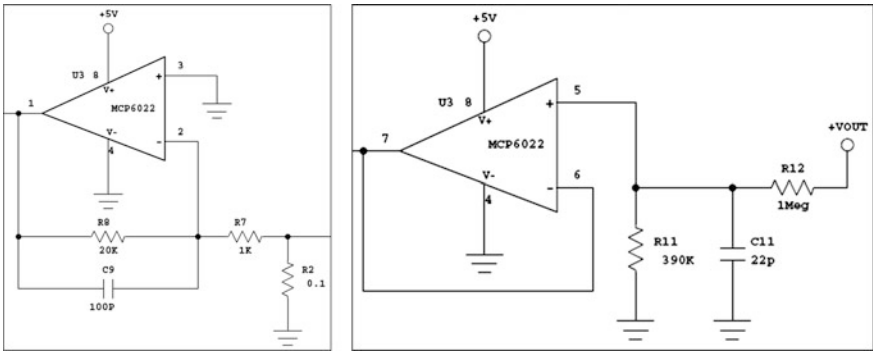

Fig. 17.31 The input current sense amplifier and the output voltage sense buffer

high. This avoids any significant current that can be drawn from the battery during eclipses via the measurement divider. The divider ratio can be again adjusted according with hardware requirements in order to maximize the dynamic range of the output voltage sensing circuitry. A buffer amplifier implemented with the second amplifier of MCP6022 is used to avoid any potential errors that may be introduced by the leakage currents of the analog input of the microcontroller. A small capacitor C11 placed in parallel with R12 forms a low-pass filter that rejects the output voltage ripple occurring at the switching frequency of the power converter.

The internal temperature sensor of the microcontroller can be used for measuring the temperature of the microcontroller's die which depends on the ambient temperature and perform a correction of the internal loop parameters (ex. the reference voltages for output voltage regulation).

17.3.1.4 The BCU Prototype

The prototype of the BCU unit is implemented in a 50 × 35 mm dual layer PCB. All components were selected with extended temperature range (−40–125 °C). The 3D representation of the prototype and associated top PCB layer are represented in Fig. 17.32.

All components are COTS and the radiations hardness tests/reports are unavailable for these components. The initial functional tests were conducted in laboratory conditions at the ambient temperature (25 °C). The PV can be simulated by placing a variable resistor (rheostat) in series with a voltage source. According with the maximum power transfer theorem, the maximum power point occurs at the half of the voltage of the voltage source.

The main switching node (source of the high-side MOSFET transistor) and the input voltage ripple waveforms are presented in Fig. 17.33.

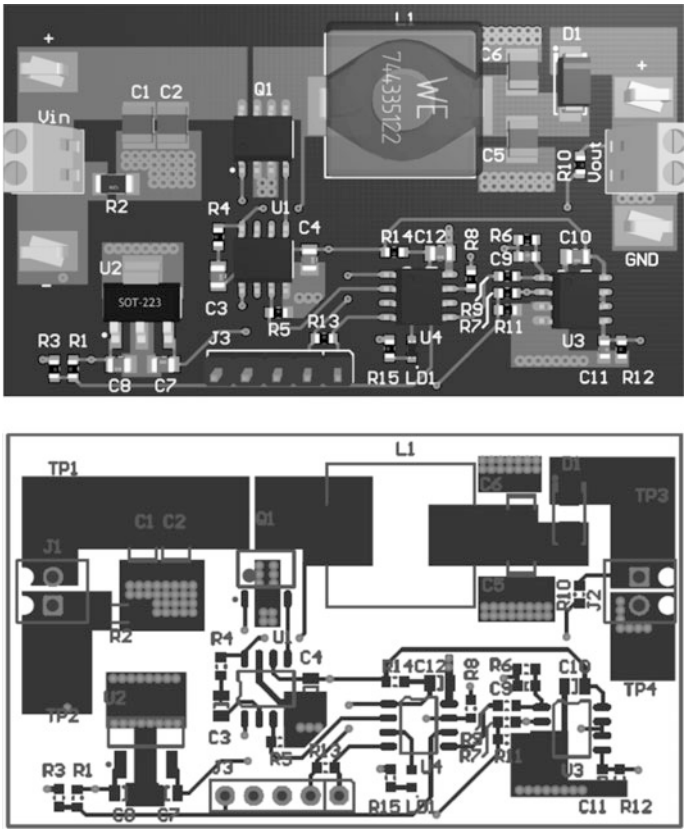

Fig. 17.32 The 3D representation of BCU board and top layer of PCB

The waveforms for output voltage ripple and input voltage perturbed by the P&O algorithm are presented in Fig. 17.34. The perturbation step is set to approximate 1% of the input voltage. The perturbation frequency is 20 Hz. The measured efficiency is 93% at maximum load.

17.3.2 The Battery Charge/Discharge Monitor Unit (BCDMU)

This unit monitors the state of the battery. Various protections like deep discharge protection and low temperature protection are implemented by this unit. The telemetry system—which reports various parameters like the battery voltage, current, stored capacity and temperature—is also implemented by this unit. The typical characteristics are listed in Table 17.7 and the block diagram is presented in Fig. 17.35.

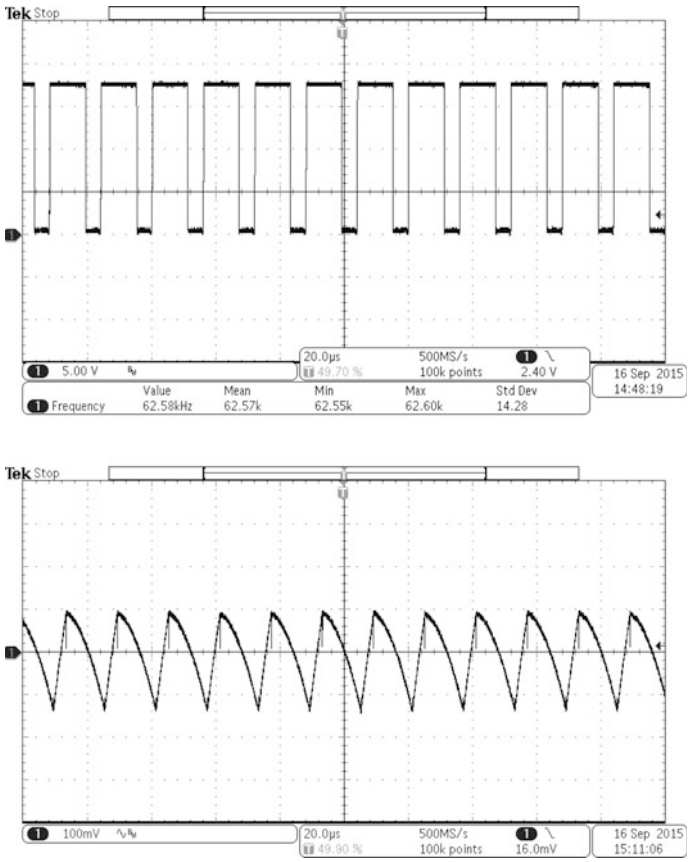

Fig. 17.33 The switch node and the input voltage ripple (BW = 20 MHz)

17.3.2.1 The Microcontroller

The BCDMU unit is controlled by a 16-bit low power microcontroller PIC24FV32KA301. This microcontroller is packaged in a 20-lead package (Fig. 17.36) and can be powered from 3.3 V (PIC24F) or 5 V (PIC24FV) sources. Notable features of this microcontroller are:

- 16-bit Modified Hardware Architecture
- 32 KB flash memory, 2 KB SRAM
- up to 16 MIPS computational power
- 8 MHz Internal Oscillator with 4x PLL Option and Multiple Divide Options
- 17-Bit by 17-Bit Single-Cycle Hardware Multiplier
- 32-Bit by 16-Bit Hardware Divider, 16-Bit × 16-Bit Working Register Array

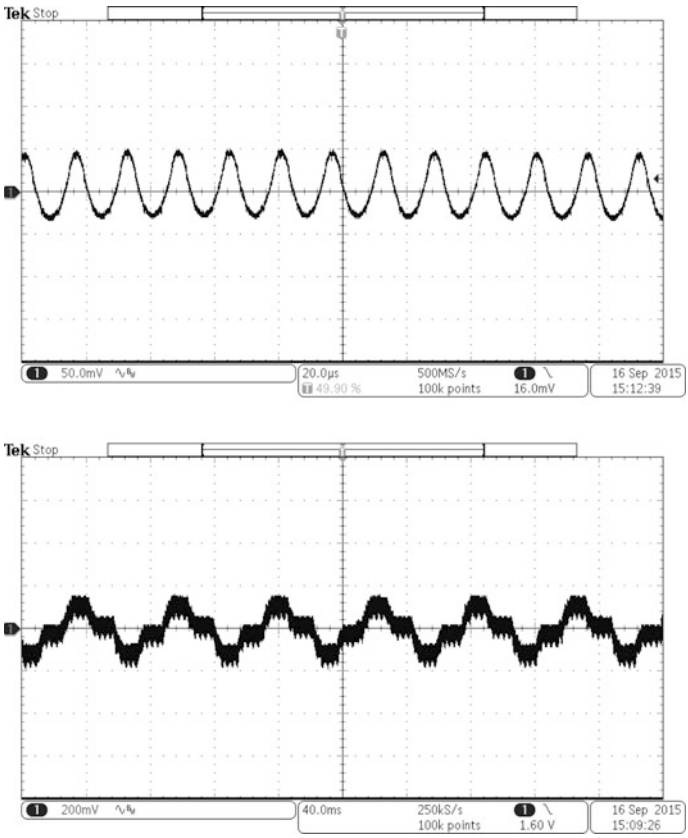

Fig. 17.34 The output voltage ripple and the input voltage perturbation during tracking phase (BW = 20 MHz)

Table 17.7 Typical electrical characteristics of BCDMU

Battery voltage range	3.6–16	V
Battery type	Li–Ion	
Maximum battery capacity	10	Ah
Maximum battery delivered current	4	A
Maximum output power	48	W
Fuse current	8	A
Maximum delivered current by the heater circuit	100	Ma

- very low power consumption (down to 8 μA, running)
- 12-Bit, Up to 16-Channel Analog-to-Digital Converter
- real-time Clock/Calendar
- operating temperature range: −40–125 °C

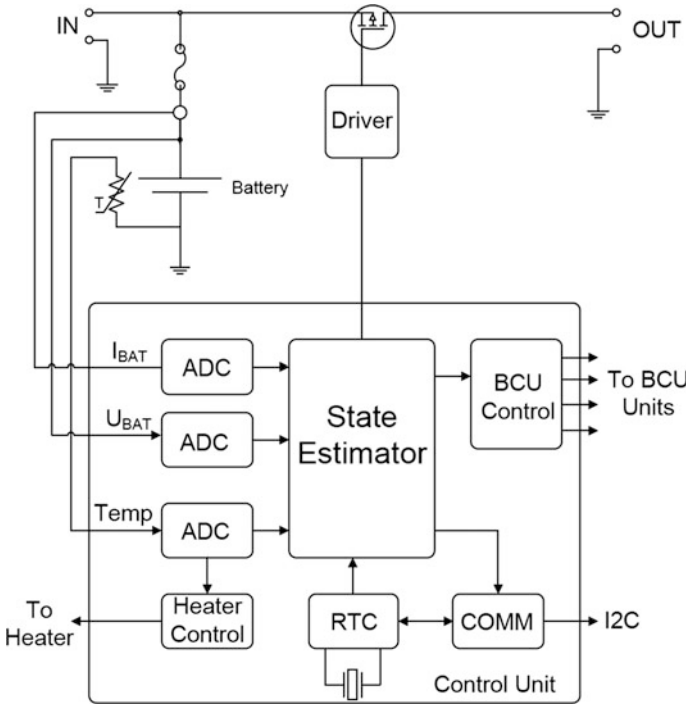

Fig. 17.35 Bloc diagram of the battery charge/discharge monitor unit

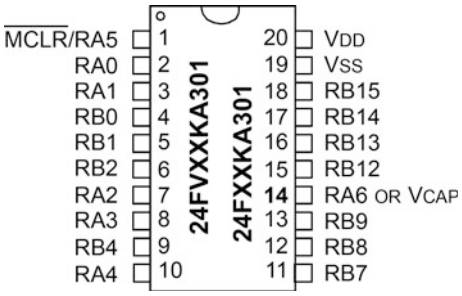

Fig. 17.36 PIC24FV16KA301 microcontroller

Measuring and reporting the battery parameters is a computational-intensive process. The presence of the hardware multiplier and divider greatly reduces the time necessary to perform various calculations. The integrated I2C controller allows the users to develop a simple and effective interface between BCDMU and central processing unit of satellite [24]. The real-time unit can be used for implementing the coulomb counting algorithm necessary for measure the battery capacity. The power consumption of this microcontroller is very low, a useful feature when the satellite enters into eclipse and the only available energy source is the battery.

17.3.2.2 The BCDMU Sensors Circuitry

BCDMU monitors three parameters of the battery: voltage, current and temperature. The parameters are used for various protections and to be reported by the telemetry system.

The battery voltage is measure the internal 12-bit Analog-to-Digital Converter (ADC) via a 4.09:1 voltage divider. The values of the resistors used to implement the voltage divide are high in order to minimize the current drawn from the battery (680 and 220 kΩ). A buffer amplifier is implemented with the OPA2170 dual rail-to-rail input/output amplifier. This buffer creates the low impedance source necessary for the microcontroller's ADC input. A snapshot of the voltage sense circuitry is presented in Fig. 17.37. Capacitors C4 and C5 are used to construct low-pass filters for avoiding the noise-induced problems.

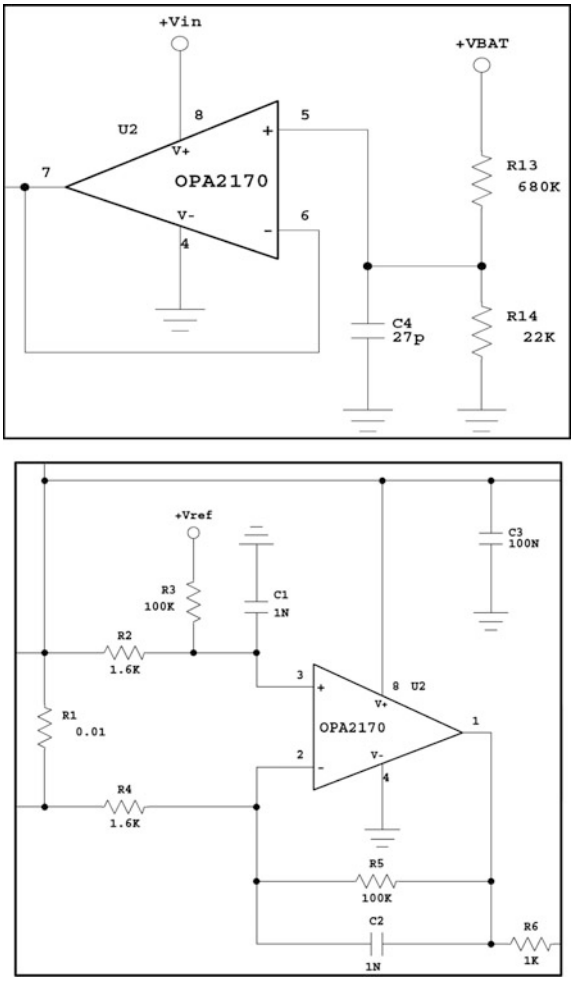

Fig. 17.37 The battery voltage measurement circuit and the current sense amplifier

The battery current is measured using a bidirectional differential amplifier. This amplifier allows the measurement of the battery current in both directions: when the battery delivers the current to the load or when the battery is charged by the BMU units. A shunt of 10 mΩ is used for the current measurement. The low value of this shunt minimizes the associated losses. The gain of differential amplifier is set to 62.5 (36 dB). By the resistors R2, R3, R4 and R5 and the output of the amplifier is centered to about 2.5 V by adding a DC offset. In order to prevent errors introduced by low Common Mode Rejection Ratio (CMMR) the gain set resistors R2, R3, R4 and R5 should be matched within 0.1%. Gain of this amplifier can be adjusted for different batteries currents for maximizing the dynamic range of the measurement circuit. A low-pass filter that rejects the high frequency noise is constructed with the aid of C1 and C2. The output of this amplifier is clamped in order to avoid damage of the microcontroller analog input using the circuit constructed with R6 and D2. For proposed prototype, the gain of the current sense amplifier is set to 0.625 V/A.

The battery temperature is measured by using a thermistor usually attached to the battery's body. The thermistor provides a very wide measurement range (usually exceeding 150 °C) and is very well suited for space applications. The output characteristic is non-linear (Fig. 17.38) and the microcontroller should perform a linearization operation for accurate temperature measurement. The thermistor used in the proposed prototype is of NTC (Negative Temperature Coefficient) type. The nominal value of this thermistor is 10 kΩ.

The equation that describes the thermistor's resistance with temperature is:

$$\frac{1}{\mathrm{T}} = \frac{1}{\mathrm{T}_0} + \frac{1}{\beta}\left(\frac{R}{R_0}\right) \tag{17.12}$$

where: T and T_0 are the ambient respective the reference temperatures (in °C), R and R_0 are the resistance and the reference resistance (specified at 25 °C), and β is a parameter specified by the thermistor manufacturer.

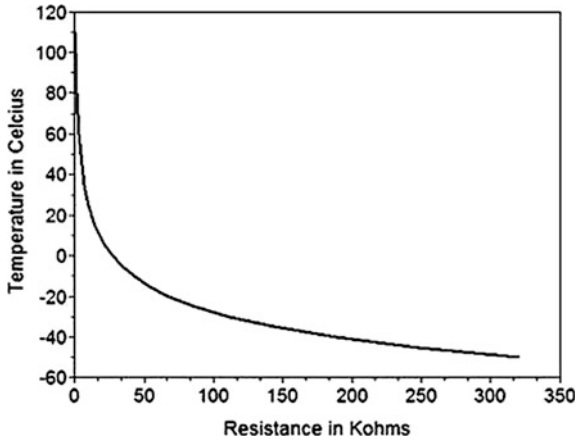

Fig. 17.38 Typical NTC thermistor characteristics

The BCDMU microcontroller will perform the linearization step by solving Eq. (17.12).

17.3.2.3 The Battery Switch

A power switch is placed between the BCDMU and the rest of the system. The role of this switch is to protect the battery against severe overload, deep discharge or accidental discharge during launch process. The power switch is implemented using a P-channel MOSFET and is activated by pulling his gate to the ground potential. The schematic of this switch is depicted in Fig. 17.39.

A resettable PTC fuse is placed in series with the battery positive terminal in order to protect against severe overcurrent that can potentially occurs if the other protections become inoperative.

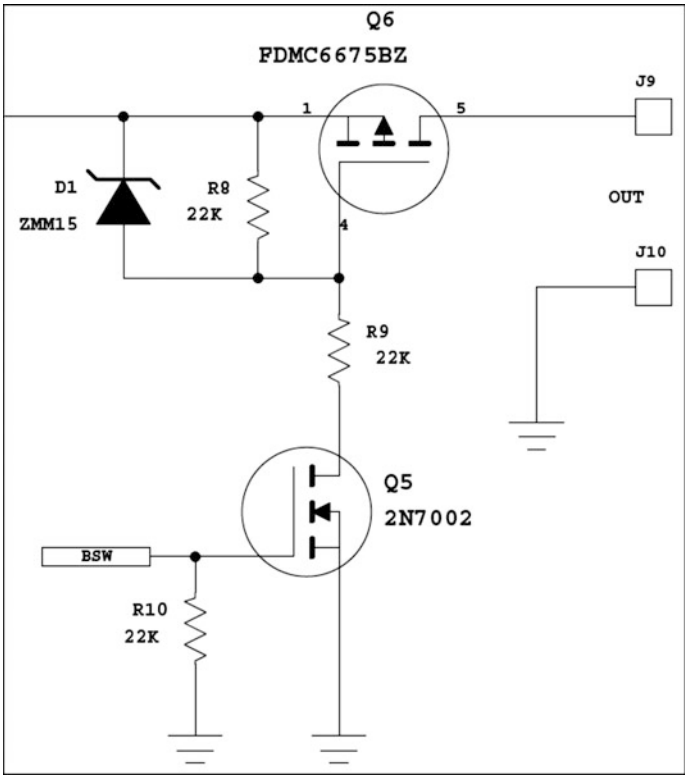

Fig. 17.39 The battery switch

17.3.2.4 The Battery Heater

If the battery's temperature drops below a certain level usually specified by manufacturer, the capacity can be severely affected. In order to prevent this phenomenon that can occurs during eclipses, the BCDMU can activate a heater circuit if the measured temperature is below a specified threshold. The heater circuit can provides up to 200 mA current and the thresholds can be programmed inside the BCDMU firmware.

17.3.2.5 Telemetry System

The Telemetry, tracking and telecommand (TT&C) system measures and reports various parameters of the battery. The parameters are available via the I2C interface provided by the BCDMU.

The I2C interface provides support for 100 or 400 kHz data rates. The number format uses the mantissa/exponent format in order to achieve good resolution without using floating point format numbers. The exponent is fixed, equal with ten [25].

Table 17.8 presents the BCDMU telemetry system set of commands.

The general packet structure is represented in Fig. 17.40. The slave address is fixed for each unit and can be set in firmware. The BCDMU firmware provides a mechanism for error detection in the form of a CRC-8 generally known as "Packet Error Check" (PEC). This PEC byte is optionally and the firmware will automatically check for the presence of this byte.

"**COM_BAT_VOLTAGE**" (0x01) command is used to read the battery voltage. The battery voltage is reported directly in volts.

"**COM_BAT_CURRENT**" (0x02) command is used to read the battery current. The battery current is reported as a signed value as the battery can deliver current during eclipses and absorb current during charging phase.

Table 17.8 Telemetry system commend list

Command	HEX code	Transmitted # bytes	Received # bytes
COM_BAT_VOLTAGE	0x01	1	2
COM_BAT_CURRENT	0x02	1	2
COM_BAT_TEMPERATURE	0x03	1	2
COM_BAT_CAPACITY	0x04	1	2
COM_BAT_STATUS	0x05	1	2

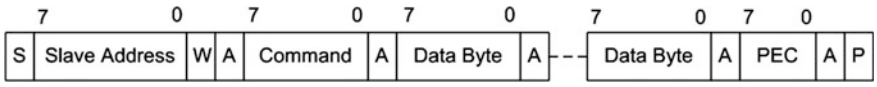

Fig. 17.40 General structure of an I2C packet of telemetry system

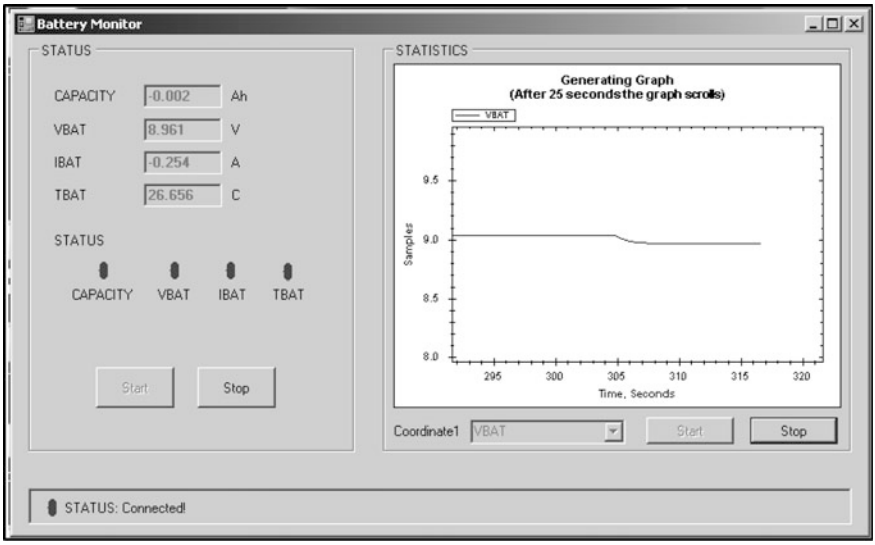

Fig. 17.41 The BCDMU PC GUI

"**COM_BAT_TEMPERATURE**" (0x03) command reads the battery's temperature. The temperature is reported directly in Celsius degrees and covers a range between −50 and 125 °C.

"**COM_BAT_CAPACITY**" (0x04) command reports the battery's current capacity. The read value is a signed number that represents the capacity directly in Ah. Before using this command, it must perform a complete charge-discharge cycle in order to calibrate the coulomb counting block of BCDMU.

"**COM_BAT_STATUS**" (0x05) command is used for fast estimation of the battery status. The number of bits on functionality of these bits can be set in the BCDMU firmware as a function of the system requirements.

A PC Graphical User Interface (GUI) was developed in order to retrieve main battery parameters from BCDMU unit. Figure 17.41 presents the GUI screen. The parameters can be plotted versus time for convenient representation.

17.3.3 The Effects of Space Radiation on Electronic Components

The space is a harsh environment. All electronic components, semiconductor materials and assemblies are affected by this environment. The main factor that causes this is the space radiation. There are four major components that form the space radiation:

- Trapped electrons found in the Van Allen Outer Belt. These are negatively charged particles with low mass but high energy (up to 7 meV). Trapped electrons can be found on orbits with high altitude like GEO (mostly telecom satellites and GPS).
- Trapped protons found in the Van Allen Inner Belt. These are positively charged particles held captive by the Earth magnetosphere. Can have energies up to 400 meV and dominates the low orbits (LEO).
- Solar particles. These are protons and heavy ions ejected from the Sun during solar flares. The energy of these particles is high enough to produce damages to electronics and the occurrence is essentially unpredictable.
- Cosmic rays. They are produced by some galactic phenomena like supernovae and contain particles with very high energy (sometimes up to 10^{20} eV). The flux is relatively low, 4 particles/cm^2/s.

There are two major categories of effects generated by space radiation on materials used for electronic devices:

- **Cumulative effects**. Long term exposure to space radiation produces a progressive degradation of semiconductor materials. There are two major effects related to long term exposure: the Total Ionization Doze (**TID**) and Displacement Damages [**DD**]. The TID is measured in grey [SI] or rad [CGI] and indicates the accumulated doze where the electrical parameters of a semiconductor device start to degrade. For radiation-hardened devices TID is between 100 krad (Si) and 1 Mrad (Si) while for COTS are between 1 krad (Si) and 100 krad (Si) (mostly below 30 krad (Si)). The displacement damages are produced by high energy particles that affect the lattice structure of the semiconductor.
- **Single event effects**. These effects are produced by a single high-energy particle that passes the semiconductor structure and disturb the normal functionality of the device. There are few categories of single event effects:
- **Single Event Upset** (**SEU**). This disturbance affects mostly the digital circuitry especially memories and is essentially non-destructive. The particle may change the state of a memory cell producing a temporary malfunction of the circuit or data loss.
- **Single Event Latch-Up** (**SEL**). This disturbance affects the circuitry that presents the latch-up phenomenon like CMOS. Essentially the particle trigger the latch-up into the semiconductor structure and the current drawn by the device may become very large and uncontrollable. The SEL can produce destructive effects unless the current drawn by device is limited.
- **Single Event Transient** (**SET**). Here the particle produces a temporary disturbance of a parameter like a voltage or current. Mostly affects the analog circuitry like the voltage regulators but may also affect indirectly the digital circuits.
- **Single Event Burnout** (**SEB**). This is the most dangerous single-event effect because produces permanent failure of the semiconductor structure. Is often

triggered by a SEL and if the current into device is not limited the temperature of the semiconductor structure will exceeds the safety limit.

For low cost, limited time space missions the cumulative effects are not a problem. However, the single event effects may severely affect the mission and some countermeasures against these effects are always necessary.

17.3.4 Countermeasures Against the Effects of Space Radiation

The cost of a space mission is very high and in this context the reliability of the electronic systems became of critical importance. A short list of specific techniques used for preventing catastrophic failure due to space radiation:

- **Use of radiation-hardened components**. These are specially developed components capable to sustain large doses of radiation without significant degradation of electrical parameters. The cost of these components is very high and the availability is limited. The typical development cycle is between five and seven years and the testing and validation effort is significant. Space agencies regularly publish documents with radiation tests done for various components.
- **Redundancy**. Redundancy is the primary option for increase the reliability of critical mission blocks or assemblies. Redundancy is obtained when more components than a specific operation needs are placed in a specific configuration so that in case that one component fails another takes instantaneously its place and the functionality is preserved. This method involves high cost and cannot be implemented for all components and assemblies for example the solar array and batteries. For very small LEO satellites this option is somehow limited by the cost and the mass/dimensions.
- **Shielding**. Shielding is an effective way to protect the electronic components against the effects produced by low-mass particles (electrons). The electronic assemblies can be covered by metal shields aluminum being the primary option due to its low mass. Shielding is not effective against large mass, high energy particles like those from the cosmic rays.

17.3.5 Reliability of Low-Cost Designs Based on COTS

The proposed PCU is entirely built with COTS. While the radiation tolerance of COTS is in most of the cases unknown there are few techniques that can improve the reliability of electronic blocks built using these components.

The redundancy is primary option also in case of low-cost designs. In case of the proposed PCU there are three functional blocks that involves redundancy:

- The Battery Charger Unit (BCU). There are four independent BCU units in this design. Each BCU is designed with a typical 30% power reserve.
- The Battery Charge/Discharge Monitor Unit (BCDMU). There are two BCDMU units that can run in parallel each one with his own battery. The telemetry system is independent for each BCDMU.
- The Isolation Unit (IU). There are two independent IU with outputs connected in parallel.

The effects induced by SEU can be minimized by using a special technique in firmware. This technique involves the use of redundant code: critical code is executed multiple times and the results are checked by a voter. The same variable is stored in three different locations and the voting system decides if this variable was affected by SEU. All constants are stored in the non-volatile memory of microcontroller and fetched before being used in code.

The most dangerous phenomenon for low-cost, COTS-based designs is SEL. SEL can produce severe malfunctions to the systems and is the primary cause for failure of these systems. The SEL can be prevented by using latch-up proof components and designs. Unfortunately most of the COTS components based on CMOS technology are not latch-up proof. In this category enters microcontrollers, volatile and non-volatile memories often used by low-cost designs. The countermeasures against SEL include:

- Use of the "Watch Dog" circuits. This circuit can reset the microcontroller in case of a malfunction produced by SEL. In order to be effective the "Watch Dog" is usually combined with other circuits like voltage supervisors.
- Use of the input current monitors. These circuits are able to detect an overcurrent that typically occurs in case of a latch-up and can be used to cycle the input power of the protected device. This kind of protection is effective against SEL and their circuitry can be implemented using radiation-hardened components.

17.4 Conclusions

In this chapter a brief overview about the characteristics and specific demands of very small satellites together with their electrical power system topologies are firstly presented. The proposed flexible hybrid power is then introduced and only the power conditioning unit that includes the battery charger unit (BCU) and the battery charge/discharge monitor unit (BCDMU) are further detailed for a specific application of a very small satellite similar to a CubeSat.

The battery charger unit (BCU) includes the DC–DC synchronous Buck converter, the digital controller implemented using a commercial, low pin count microcontroller and the BCU sensors' circuitry that monitors three parameters: input voltage (panel voltage), input current (panel current) and the output battery's

voltage. The input voltage and the input current are used for the MPPT implementation of the P&O algorithm and the output voltage is used for the implementation of the battery-specific charging algorithm. At the end of this subchapter, the BCU prototype is explained from the practical perspective of the built prototype.

The battery charge/discharge monitor unit (BCDMU) contains at its turn a 16-bit low power microcontroller, the BCDMU's sensors circuitry that monitors other three battery parameters: voltage, current and temperature, the battery switch power whose role is to protect the battery against severe overload, deep discharge or accidental discharge during the launch process, the battery heater activated during eclipses in order to prevent battery's temperature drops below a certain level and finally the telemetry, tracking and telecommand (TT&C) system that measures and reports various parameters of the battery available via the I2C interface provided by the BCDMU. The blocks described above are completely functional, being the subject of a national program, according to acknowledgements below.

Acknowledgements This work was supported by a grant of the Romanian National Authority for Scientific Research, Program for research Space Technology and Advanced Research - STAR, project number 80/29.11.2013.

References

1. https://en.wikipedia.org/wiki/Satellite
2. https://en.wikipedia.org/wiki/Miniaturized_satellite
3. http://space.stackexchange.com/questions/5676/aocs-for-very-small-satellites-micro-nano-pico-femto
4. http://www.nasa.gov/mission_pages/smallsats/
5. http://arc.aiaa.org/doi/abs/10.2514/1.28678?journalCode=jsr
6. Patel MR (2005) Spacecraft power systems. CRC Press, Boca Raton
7. https://www.itu.int/dms_pub/itu-r/opb/rep/R-REP-SA.2312-2014-MSW-E.docx
8. Martin L, Jones WH, Shiroma WA (2014) Small-satellite projects offer big rewards. IEEE Potentials 33(4):24–30
9. http://www.esa.int/Our_Activities/Space_Engineering_Technology/Technology_CubeSats
10. Strain A (2010) User manual: CubeSat 1U electronic power system and batteries: CS-1UEPS2-NB/-10/-2. Clyde Space Ltd
11. http://www.clyde-space.com/
12. Surampudi R, Hamilton T, Rapp D (2002) Solar cell and array technology for future space science missions, June 2002, NASA, pp 1–100
13. De Luca A (2011) Architectural design criteria for spacecraft solar arrays (Chap 8) in solar cells—thin-film technologies. InTech Publishing House, Vienna. ISBN 978-953-307-570-9
14. Colasanti S, Nesswetter H, Zimmermann CG, Lugli P (2014) Modeling and parametric simulation of triple junction solar cell for space applications. In: IEEE 40th photovoltaic specialist conference (PVSC 2014), pp 1784–1789
15. Pearson C, Thwaite C, Russel N (2005) Small cell lithium-ion batteries: the responsive solution for space energy storage. In: American institute of aeronautics and astronautic (AIAA) 3rd responsive space conference, 25–28 April 2005, Los Angeles, USA

16. Olsson D (1993) A power system design for a microsatellite. In: ESA/ESTeC, European space power conference, 23–27 August 1993, Graz, Austria
17. Oprea S, Tanase MC, Florescu A (2012) PV charger system using a synchronous buck converter. In: Proceedings of SNET2012, 14 December 2012, Bucharest, Romania, vol 3(1), pp 328–333. ISSN 2067-4147
18. Castaner L, Silvestre S (2002) Modelling photovoltaic systems using PSpice. Wiley, New York. ISBN 978-0-470-84527-1
19. Esram T, Chapman JR (2007) Comparison of photovoltaic array maximum power point tracking techniques. IEEE Trans Energy Convers 22(2):439–449 ISSN 0885–8969
20. Femia N, Petrone G, Spagnuolo G, Vitelli M (2012) Power electronics and control techniques for maximum energy harvesting in photovoltaic systems. CRC Press, Boca Raton. ISBN 9781466506909
21. Sera D, Mathe L, Kerekes T, Spataru SV, Teodorescu R (2013) On the perturb-and-observe and incremental conductance MPPT methods for PV systems. IEEE J Photovoltaics 3 (3):1070–1078
22. Demirel S, Sanli E, Gokten M, Yagli AF (2012) Properties and performance comparison of electrical power sub-system on TUSAT communication satellite. In: 2012 IEEE first AESS European conference on satellite communications (ESTEL 2012), 2–5 October 2012, Italy, Rome. Print ISBN:978-1-4673-4687-0
23. Erickson RW, Maksimovic D (2001) Fundamentals of power electronics, 2nd edn. Springer, New York. ISBN 13: 978-1475705591
24. Oprea S, Rosu-Hamzescu M, Radoi C (2014) Implementation of simple MPPT algorithms using low-cost 8-bit microcontrollers. In: IEEE conference on electronics, computers and artificial intelligence (ECAI 2014), 23–25 October 2014, pp 31–34
25. Rosu-Hamzescu M, Oprea S (2012) High-power CC/CV battery charger using an inverse SEPIC (Zeta) topology. Microchip Technology Inc., AN1467, pp 1–16